Title	Benchmarking of flux-driven full-F gyrokinetic simulations
Author(s)	Asahi Yuichi, Grandgirard V., Idomura Yasuhiro, Garbet X., Latu G., Sarazin Y., Dif-Pradalier G., Donnel P., Ehrlacher C.
Citation	Physics of Plasmas, 24(10), 102515 (2017)
Text Version	Publisher
URL	https://jopss.jaea.go.jp/search/servlet/search?5060888
DOI	https://doi.org/10.1063/1.4998015
Right	© 2017 American Institute of Physics. This article may be downloaded for personal use only. Any other use requires prior permission of the author and AIP Publishing. The following article appeared in Physics of Plasmas, 24(10), 102515 (2017) and may be found at https://doi.org/10.1063/1.4998015.

Benchmarking of flux-driven full-F gyrokinetic simulations

Yuuichi Asahi, Virginie Grandgirard, Yasuhiro Idomura, Xavier Garbet, Guillaume Latu, Yanick Sarazin, Guilhem Dif-Pradalier, Peter Donnel, and Charles Ehrlacher

Citation: Physics of Plasmas **24**, 102515 (2017);

View online: https://doi.org/10.1063/1.4998015

View Table of Contents: http://aip.scitation.org/toc/php/24/10

Published by the American Institute of Physics

Benchmarking of flux-driven full-F gyrokinetic simulations

Yuuichi Asahi,[1,2,a)] Virginie Grandgirard,[1] Yasuhiro Idomura,[2] Xavier Garbet,[1] Guillaume Latu,[1] Yanick Sarazin,[1] Guilhem Dif-Pradalier,[1] Peter Donnel,[1] and Charles Ehrlacher[1]
[1]*CEA, IRFM, F-13108 Saint-Paul-lez-Durance, France*
[2]*Japan Atomic Energy Agency, 178-4-4 Wakashiba, Kashiwa, Chiba, Japan*

(Received 28 July 2017; accepted 2 October 2017; published online 20 October 2017)

Two full-F global gyrokinetic codes are benchmarked to compute flux-driven ion temperature gradient (ITG) turbulence in tokamak plasmas. For this purpose, the Semi-Lagrangian code GYrokinetic SEmi-LAgrangian and the Eulerian code GT5D are employed, which solve the full-F gyrokinetic equation with a realistic fixed flux condition. The equilibrium poloidal flow profile formation processes are benchmarked and compared against the local neoclassical theory. The simulations above are carried out without turbulence, which agree well with each other and with the theoretical estimates. Here, a lot of attention has been paid to the boundary conditions, which have huge impacts on the global shape of radial electric field. The behaviors of micro-instabilities are benchmarked for linear and nonlinear cases without a heat source, where we found good agreements in the linear growth rates and nonlinear critical gradient level. In the nonlinear case, initial conditions are chosen to be identical since they dominate the transient turbulence behavior. Using the appropriate settings for the boundary and initial conditions obtained in the benchmarks above, a flux-driven ITG turbulence simulation is carried out. The avalanche-like transport is assessed with a focus on spatio-temporal properties. A statistical analysis is performed to discuss this self-organized criticality (SOC) like behaviors, where we found a $1/f$ spectra and a transition to $1/f^3$ spectra at high-frequency side in both codes. Based on these benchmarks, it is verified that the SOC-like behavior is robust and not dependent on numerics. *Published by AIP Publishing.*
https://doi.org/10.1063/1.4998015

I. INTRODUCTION

First-principles kinetic simulations are considered as essential tools to understand and predict plasma transport phenomena in magnetic confinement fusion devices. So far, a number of simulation studies have addressed the physical mechanisms involved in turbulent transport, and compared them with experimental results (see the review paper,[1] for example). In most cases, these codes tackle local transport phenomena under fixed plasma profiles. Since they compute the perturbed part of the distribution functions only, they are often called local δf gyrokinetic simulations. Tremendous efforts have been done for code verification, namely, benchmarking of different local δf gyrokinetic codes, in order to ensure better credibility.[2,3]

Concerning the experimental situation, the local approach may fail whenever the characteristic size of turbulence is non-negligible compared with the machine size or the profile formation is affected by plasma turbulence itself, possibly leading to an organization of meso-scale structures. Robust features of non-local transport have been reported.[4,5] To address this issue, a new generation of gyrokinetic codes called full-F gyrokinetic codes have been developed, where the fluctuations and equilibrium profiles evolve self-consistently.[6–10] More importantly, full-F gyrokinetic codes can compute turbulent heat transport in the presence of a physically relevant fixed flux condition.

In addition, full-F gyrokinetics is an approach to treat turbulent and collisional transport consistently. This favorable feature is rather problematic in benchmarking due to the complex physics involved in these simulations. In fact, there exist few benchmark works of full-F gyrokinetic codes[11] and they are addressing fixed-gradient global simulations with adaptive heat source terms[12] rather than a realistic heat source term with a constant heating source. In order to address the complicated dynamics of full-F flux-driven simulations, we first decompose the problem into subsets, each tackling a specific physics issue. For collisional (neoclassical) properties, we carried out simulations where the Ion Temperature Gradient (ITG) mode is stable so that transport is only due to collisions. For turbulence, we investigated linear ITG mode and nonlinear decaying ITG turbulence in the absence of collisions (or weakly collisional). After completing these tests, we move to the benchmark of flux driven ITG turbulence, which involves all the physical processes listed above. The physics to be addressed mainly is the avalanche-like transport and profile corrugations and their statistical properties. We focus on the self-organized criticality (SOC) like behaviors, which are at the heart of the full-F flux driven gyrokinetic simulations. It should be stressed that these physical processes can only be simulated in the framework of global full-F gyrokinetic models.

This paper contributes to the benchmark of long-time flux-driven ITG turbulence simulations, which is organized as follows: Section II describes the full-F gyrokinetic model with source and sink terms. In Sec. III, the differences in the

[a)]Electronic mail: yuuichi.asahi@cea.fr

numerical schemes are shown. The benchmarks for the neoclassical physics and zonal flow dynamics against theories are shown in Sec. IV. The linear and nonlinear benchmarks for gyrokinetics without source and sink terms are shown in Sec. V. The benchmark for the flux driven case is summarized in Sec. VI. The results are summarized in Sec. VII.

II. MODEL

In this section, we briefly describe the physical models used in GYrokinetic SEmi-LAgrangian (GYSELA)[9,13] and GT5D[10] codes. Although these codes can now treat the kinetic electrons,[14] we employ the conventional versions with adiabatic electrons in this work. Since the gyrokinetic part is fundamentally the same, we emphasize the differences in the collision operators and sink/source models.

A. Full-F gyrokinetic models

In the modern gyrokinetic theory,[15] the time evolution of the guiding center distribution function f can be computed by the 5D gyrokinetic equation

$$\frac{\partial \mathcal{J} f}{\partial t} + \nabla \cdot \mathcal{J} \dot{\mathbf{R}} f + \frac{\partial \mathcal{J} \dot{v}_\parallel f}{\partial v_\parallel} = \mathcal{J}(\mathcal{D}_r(f) + \mathcal{K}(f) + \mathcal{C}(f) + S), \tag{1}$$

where $\mathcal{J} = m_i^2 B_\parallel^*$ is the Jacobian in the gyrocenter coordinate and $v_\parallel$ is the parallel velocity. m_i is the mass of ion, $B_\parallel^* = \mathbf{b} \cdot \mathbf{B}^*$ is the parallel component of $\mathbf{B}^*$, with the unit vector in the parallel direction $\mathbf{b}$, and $\mathbf{B}^* = \mathbf{B} + (B v_\parallel / \Omega_i) \nabla \times \mathbf{b}$. $\Omega_i = (e_i B)/(m_i c)$ is the ion cyclotron frequency with the charge of ion e_i and the speed of light c. For the right hand side, $\mathcal{D}_r$ and $\mathcal{K}$ are a diffusion term and a Krook operator applied on radial buffer regions, $\mathcal{C}$ represents a collision operator, and S is a source term. The details for the collision operator are defined in Sec. II B, and source/sink terms (diffusion or Krook) are described in Secs. II C and II D.

The nonlinear characteristics in Eq. (1) are given by

$$\begin{aligned} \dot{\mathbf{R}} \equiv \{\mathbf{R}, H\} &= \frac{\mathbf{B}^*}{m_i B_\parallel^*} \frac{\partial H}{\partial v_\parallel} + \frac{c}{e_i B_\parallel^*} \mathbf{b} \times \nabla H \\ &= v_\parallel \mathbf{b} + \frac{c}{e_i B_\parallel^*} \left(e_i \nabla \langle \phi \rangle_\alpha + m_i v_\parallel^2 \mathbf{b} \cdot \nabla \mathbf{b} + \mu \nabla B \right), \end{aligned} \tag{2}$$

$$\begin{aligned} \dot{v}_\parallel \equiv \{v_\parallel, H\} &= -\frac{\mathbf{B}^*}{m_i B_\parallel^*} \cdot \nabla H \\ &= -\frac{\mathbf{B}^*}{m_i B_\parallel^*} \cdot \left(e_i \nabla \langle \phi \rangle_\alpha + \mu \nabla B \right), \end{aligned} \tag{3}$$

where $\{F, G\}$ is the gyrokinetic Poisson bracket operator

$$\begin{aligned} \{F, G\} \equiv \frac{\Omega_i}{B} \left(\frac{\partial F}{\partial \alpha} \frac{\partial G}{\partial \mu} - \frac{\partial F}{\partial \mu} \frac{\partial G}{\partial \alpha} \right) + \frac{\mathbf{B}^*}{m_i B_\parallel^*} \\ \times \left(\nabla F \frac{\partial G}{\partial v_\parallel} - \frac{\partial F}{\partial v_\parallel} \nabla G \right) - \frac{c}{e_i B_\parallel^*} \mathbf{b} \cdot \nabla F \times \nabla G \end{aligned} \tag{4}$$

in the gyro-center coordinates $\mathbf{Z} = (\mathbf{R}, v_\parallel, \mu, \alpha)$, where μ is the magnetic moment and α is the gyro-phase angle. H represents the Hamiltonian of the system defined as

$$H = \frac{1}{2} m_i v_\parallel^2 + \mu B + e_i \langle \phi \rangle_\alpha. \tag{5}$$

Here, $\langle \phi \rangle_\alpha = \oint \phi \mathrm{d}\alpha / 2\pi$ stands for the gyro-averaged electrostatic potential ϕ.

The electrostatic potential ϕ is determined by the quasi-neutrality condition

$$\begin{aligned} -\nabla_\perp \cdot \frac{\rho_{\mathrm{ti}}^2}{\lambda_{\mathrm{Di}}^2} \nabla_\perp \phi + \frac{1}{\lambda_{\mathrm{De}}^2} \left(\phi - \langle \phi \rangle_f \right) \\ = 4\pi e_i \left[\int f \delta([\mathbf{R} + \boldsymbol{\rho}] - \mathbf{x}) \mathrm{d}^6 Z - n_{\mathrm{G,eq}} \right], \end{aligned} \tag{6}$$

where $\mathbf{R} + \boldsymbol{\rho}$ is a particle position, $\mathrm{d}^6 Z = m_i^2 B_\parallel^* \mathrm{d}\mathbf{R} \mathrm{d}v_\parallel \mathrm{d}\mu \mathrm{d}\alpha$ is the phase space volume of the gyro-center coordinates, ρ_{ti} is the Larmor radius evaluated with the thermal velocity v_{ti}, λ_{Di} and λ_{De} are the ion and electron Debye lengths, $\langle \cdot \rangle_f$ is a flux surface average, and $n_{\mathrm{G,eq}}$ is the equilibrium guiding-center density. The first term of the left hand side stands for the ion polarization density in the long wavelength approximation. This assumption should be valid for the core ITG turbulence, which is characterized by $k_\perp \rho_{\mathrm{ti}} \ll 1$ with the perpendicular wavenumber $k_\perp$. By coupling the gyrokinetic equation (1) and quasi-neutrality condition (6), the gyrokinetic model can be solved self-consistently.

B. Collision operators

In this subsection, we briefly describe the collision operators used in GYSELA[13] and GT5D.[16] Although there are some differences, it has been shown that the conservative properties[13,16] and some neoclassical properties[17,18] are satisfied in both codes. It should be noted that the finite-Larmor-radius (FLR) effect is not taken into account in the collision operators in GYSELA and GT5D, which is equivalent to a collision operator computed in the drift-kinetic limit.

1. Collision operator in GYSELA

The version of the collision operator considered in the present study for GYSELA (other versions exist, such as a recently benchmarked multi-species version[19,20]) is given by a simplified Lenard-Bernstein collision operator,[21] where only the $v_\parallel$ contribution is taken into account

$$C(f) = \frac{1}{B_\parallel^*} \frac{\partial}{\partial v_\parallel} \left[B_\parallel^* \left(\mathcal{D}_\parallel \frac{\partial f}{\partial v_\parallel} - \mathcal{V}_\parallel f \right) \right]. \tag{7}$$

The operators $\mathcal{D}_\parallel$ and $\mathcal{V}_\parallel$, respectively, model a diffusion and a drag in the parallel velocity direction. The conservation properties of parallel momentum and energy are ensured by constraining $\mathcal{D}_\parallel$ to depend on μ only and defining the local fluid velocity $V_{\parallel,\mathrm{coll}}$ and ion temperature T_{coll} in an appropriate manner.[13]

2. Collision operator in GT5D

GT5D is equipped with the linearized Fokker-Planck collision operator[22] as $C(f) = C_{\mathrm{T}}(f) + C_{\mathrm{F}}$. The test particle operator C_{T} is given by

$$C_{\mathrm{T}}(f) = \frac{\partial}{\partial s}\left(\nu_{\perp 1} v^2 f\right) + \frac{\partial}{\partial u}\left(\nu_{\parallel 1} u f\right) + \frac{1}{2}\frac{\partial^2}{\partial s^2}\left(\nu_{\perp 2} v^4 f\right) + \frac{1}{2}\frac{\partial^2}{\partial u^2}\left(\nu_{\parallel 2} v^2 f\right) + \frac{\partial^2}{\partial s \partial u}\left(\nu_{\parallel \perp} v^3 f\right), \quad (8)$$

where $s = 2\mu B/m_i$ and $u = v_\parallel - U_\parallel$ are defined in a moving frame with respect to the parallel flow velocity $U_\parallel$ and $v^2 = u^2 + s$. The field particle operator C_{F} ensures the conservation properties of parallel momentum and energy. The definitions of the collision frequencies, $\nu_{\perp 1}$, $\nu_{\parallel 1}$, $\nu_{\perp 2}$, $\nu_{\parallel 2}$, $\nu_{\parallel \perp}$, and the field particle operator C_{F} are given in the Appendix of Ref. 16.

C. Source models

Let us describe the gyrokinetic equation neglecting all terms but the source term

$$\frac{\partial f}{\partial t} = S_{\mathrm{src}}. \quad (9)$$

We assume that the source term can be expressed in the following way:

$$S_{\mathrm{src}} = S_0 S_E(\rho, E) S_r(\rho), \quad (10)$$

where S_0 is the amplitude of the source in physical unit, $E = v_\parallel^2/2 + \mu B$ is the dimensionless energy, and S_E and S_r represent source profiles in velocity space and real space, respectively. $\rho = r/a$ is the normalized minor radius used as a radial variable throughout the paper, with a minor radius a. In GYSELA and GT5D, the radial and velocity space profiles (all variables are dimensionless) are given by

$$S_{r,\mathrm{GYS}}(\rho) = -\frac{1}{2}\left[\tanh\left(\frac{\rho - \rho_s - 3L_s}{L_s}\right) + \tanh\left(\frac{\rho_s - 3L_s - \rho}{L_s}\right)\right],$$

$$S_{r,\mathrm{GT5D}}(\rho) = \frac{1}{2}\left[1 - \tanh\left(\frac{\rho - \rho_s}{L_s}\right)\right],$$

$$S_{E,\mathrm{GYS}}(\rho, E) = \frac{1}{3\pi\sqrt{2\pi}T_s^{5/2}}\left(\frac{E}{T_s} - \frac{3}{2}\right)\exp\left[-E/T_s\right], \quad (11)$$

$$S_{E,\mathrm{GT5D}}(\rho, E) = \frac{B_0}{B_\parallel^*}\left[f_{\mathrm{M1}} - f_{\mathrm{M2}}\right], \quad (12)$$

where f_{M1} represents the Maxwellian

$$f_{\mathrm{M1}} = \frac{1}{\left(2\pi\bar{T}_1\right)^{3/2}}\exp\left[-E/2\bar{T}_1\right] \quad (13)$$

for the volume averaged temperature $\bar{T}_1$ and f_{M2} is for the volume averaged temperature $\bar{T}_2$. If we take $\bar{T}_2 = \bar{T}_1 - \Delta T$, Eq. (12) can be approximated by

$$S_{E,\mathrm{GT5D}}(\rho, E) \simeq \frac{B_0}{B_\parallel^*}\left[\frac{\partial f_{\mathrm{M1}}}{\partial T}\Delta T\right] = \frac{B_0}{B_\parallel^*}\left[f_{\mathrm{M1}}\frac{\partial \ln f_{\mathrm{M1}}}{\partial T}\Delta T\right]. \quad (14)$$

If we neglect the difference in B_0 and $B_\parallel^*$, of the order of the inverse aspect ratio $\epsilon = r/R_0$ and use the relationship $\ln f_{\mathrm{M1}} = -3/2 \ln T_1 - E/T_1$, it leads to

$$S_{E,\mathrm{GT5D}}(\rho, E) \simeq C\frac{f_{\mathrm{Ms}}}{T_s}\left(\frac{E}{T_s} - \frac{3}{2}\right) \quad (15)$$

by replacing T_1 by T_s. Since the difference in $B_\parallel^*$ and B is of the order of $\rho_\star$ and negligible, the major difference between B_0 and $B_\parallel^*$ is of the order of the inverse aspect ratio ϵ, that is the difference between B and B_0. In our flux-driven test case with a relatively large aspect ratio (see Table III), the difference in B_0 and $B_\parallel^*$ is about 10% in the source region, since the source term is strongly localized in the $\rho < 0.3$ region, wherein ϵ is smaller than 0.1. Although this gives the minor difference in the region with $\rho < 0.3$, it may not affect much in the region with $0.3 < \rho < 1.0$ since the integrated input power which affects the dynamics in this region is the same for both codes. On one hand, the GYSELA source model has isotropic velocity space structure, but it gives a momentum input due to the velocity space Jacobian found in Eq. (1). On the other hand, the GT5D source model does not impose any extra momentum input, at the cost of anisotropic velocity space structure. The impact of momentum input is of the order of $\rho_\star$, but it could be important when discussing the parallel flow dynamics, as found in Sec. VI. Equation (15) is the same as Eq. (11) except for the factor C. The difference is then absorbed in the source amplitude S_0. Figure 1 shows the radial and velocity space profiles of source terms used in this study. For radial profile, we set $\rho_s = 0.01212$ and $L_s = 0.1$ in GYSELA and $\rho_s = 0.31$ and $L_s = 0.1$ in GT5D. For the velocity space, we employ $T_s = 1.5T_0$ and $\Delta T = 0.1T_0$ in order to make the velocity space structures the same in both codes in case we dismiss the difference in $B_\parallel^*$ and B_0. Here, T_0 is the reference temperature at the mid-minor radius (see Sec. III D for detail). These parameters are used in the flux-driven simulations in Sec. VI.

As is clear from Eq. (11), this source term continuously reduces the number of slow particles and increases the number of fast particles. This process leads to plasma heating. This is different from a Krook-type source term as used in Ref. 12, which forces the temperature profile to be fixed on average.

D. Sink models

In practice, GYSELA often employs diffusion terms in the buffer regions as a sink term (although a Scrape-Off-Layer (SOL)-like outer boundary condition has been recently developed[23]). However, for better comparison with GT5D, we used a Krook type operator $\mathcal{K}_r(f) = -\nu(\rho)(f - f_{\mathrm{M}})$ in GYSELA as well as GT5D. The radial profile of the coefficient $\nu(\rho)$ is given by

$$\nu(\rho) = \nu_0\left[1 + \frac{1}{2}\tanh\left(\frac{\rho - \rho_k}{L_k}\right)\right], \quad (16)$$

where ν_0 is the diffusion coefficient, ρ_k and L_k are, respectively, the location and the steepness of the buffer regions. For the flux-driven simulations in Sec. VI, we employ $\rho_k = 1.0$, $L_k = 0.1$, and $\nu_0 a/v_{\mathrm{ti}} = 0.1$. The Krook operator forces the distribution function to relax towards the initial Maxwellian f_{M} in the buffer region. Thus, turbulence is damped in the buffer region.

III. NUMERICAL SCHEMES

In this subsection, we briefly describe the numerical schemes used in the codes. We will focus, in particular, on

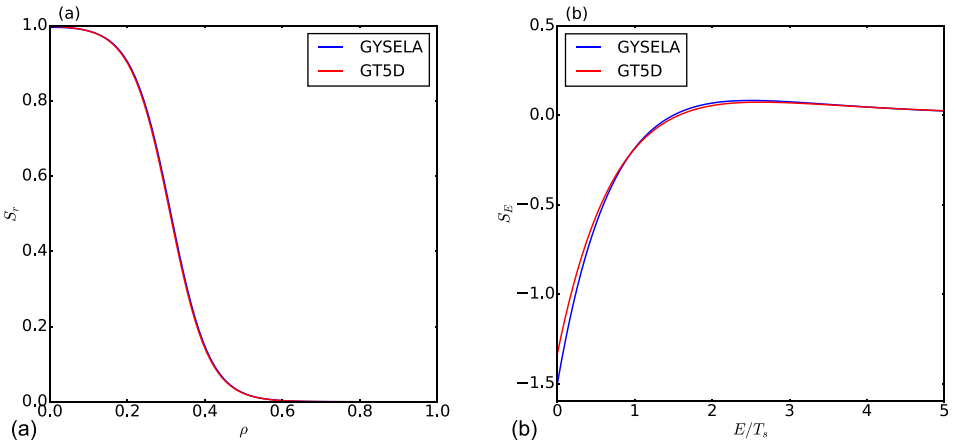

FIG. 1. Profiles of source terms in GYSELA and GT5D. (a) Radial structure and (b) Velocity space structure.

some differences that involve different numerical properties which could end up with different results. For example, the numerical schemes to solve the gyrokinetic Poisson equation, which are relevant to the boundary conditions, may have a strong impact on the global mode structure of the electrostatic potential. The comparisons of numerical costs are provided in the Appendix.

A. GYSELA code

As named, GYSELA (GYrokinetic SEmi-LAgrangian) code uses a Backward Semi-Lagrangian scheme to solve the advection term. In order to avoid a costly multidimensional interpolation, the advection operator is split into three different operators based on Strangs's operator decomposition method:[24] 2D (r,θ) + 1D $(v_\parallel)$ + 1D (φ) advection terms. Here, GYSELA employs the toroidal coordinate system (r,θ,φ) for a spatial coordinate and $(v_\parallel,\mu)$ for a velocity space coordinate. The Poisson equation is solved with Fourier expansion in toroidal and poloidal directions and finite differences in the radial direction. The difficulty lies in the estimate of flux surface averaged electrostatic potential $\langle\phi\rangle_f$, since this term is nonlinear in θ due to the θ dependence of the Jacobian. To tackle this, the Poisson equation is decomposed in two equations, one for the difference between the potential and its flux surface average and the other for the flux surface averaged component. These equations can be solved sequentially, and finally, the electrostatic potential can be obtained. The boundary conditions used in these equations are described in Sec. III C.

Contrary to local flux-tube codes, the gyro-averaging operation is not straightforward. In the flux-tube codes, the gyro-average operator can be represented by a Bessel function in the Fourier space based on the periodicity assumptions both in radial and poloidal directions (that is the local approach). In a global code, a periodic boundary condition in the radial direction is not allowed so that the Fourier representation of the gyro-average operator is no longer feasible. Therefore, we have to compute the gyro-average operator numerically in real space with some approximations. In GYSELA, there are two possibilities to approximate the gyro-average: A Padé approximation and integration on gyro-circles using Hermite interpolation. Here, we employ the Hermite interpolation approach with 8 sampling points. The time integration is performed using a predictor-corrector method. The detailed implementation of GYSELA is found in Ref. 13.

B. GT5D code

In GT5D, the gyrokinetic Poisson bracket operator is discretized using the fourth-order non-dissipative and conservative finite difference scheme,[10] which is a variant of the Morinishi scheme[25] extended to incompressible Hamiltonian flows, and the gyrokinetic Poisson equation Eq. (6) is computed using a toroidal mode expansion and a 2D finite element approximation on the poloidal plane. Similar to GYSELA, the gyro-average is evaluated by a finite-point sampling technique, with 40 sampling points. GT5D solves the gyrokinetic Vlasov equation in the cylindrical coordinate (R,Z,φ) and the gyrokinetic Poisson equation in the flux coordinates (ψ,θ^*,φ), with the poloidal flux ψ and the straight-field-line poloidal angle θ^*. The velocity space coordinate is uniform in $(v_\parallel,w)$ directions, with $w=(2B_0\mu/m_i)^{1/2}=(B_0/B)^{1/2}v_\perp$. The use of an aligned coordinate in the w direction is beneficial to capture trapped-passing boundaries.

The time integration is performed using the second-order additive semi-implicit Runge-Kutta method and a stiff linear term involving the parallel streaming is treated implicitly. An implicit part is solved using the generalized conjugate residual method. The detailed implementation of GT5D is found in Refs. 10 and 16.

C. Boundary conditions

Due to the differences in the numerical schemes used to solve the Poisson equation, GYSELA and GT5D impose different boundary conditions on electric potential ϕ. The non-axisymmetric components of ϕ are forced to be zero at both inner (if exists) and outer boundaries in both codes. The axisymmetric ϕ_{00} mode is treated in a different way. In GT5D, the Dirichlet boundary condition $\phi_{00}=0$ is applied at the edge, while the natural boundary condition is imposed at the magnetic axis. It should be noted that the use of cylindrical coordinates (R,Z,φ) in GT5D allows one to avoid the singularity at the magnetic axis. In GYSELA, the plasma region $\rho_{\min}<\rho(=r/a)<\rho_{\max}$, with some tiny value $\rho_{\min}$ is solved in order to avoid the singularity in $1/r$ at the magnetic

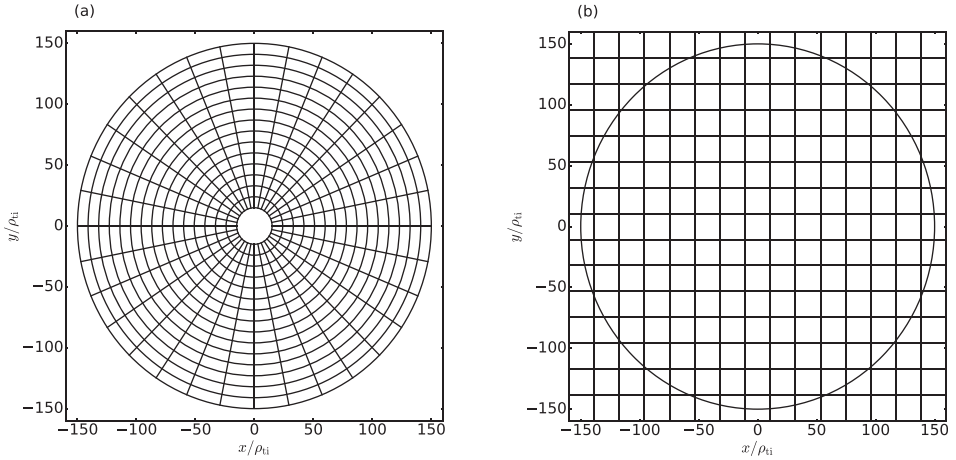

FIG. 2. Mesh grids in GYSELA (a) and GT5D (b). Although emphasized by setting $\rho_{min} = 0.1$ in figure (a), the actual hole inside the inner boundary is rather small with $\rho_{min} = 0.01$ even with the Neumann condition.

axis.[13] Conventionally, for the axisymmetric ϕ_{00} mode, the Dirichlet boundary condition is imposed at the edge ($\rho = \rho_{max}$), while the Dirichlet or Neumann conditions can be chosen at the inner boundary ($\rho = \rho_{min}$). The Neumann boundary condition can be applied only with $\rho_{min} \leq 10^{-2}$, which ensures that the poloidal dependence of the Jacobian is negligible. Recently, we employed the scheme in Ref. 26 to avoid imposing any boundary condition at the inner boundary ($\rho = \rho_{min}$). In this scheme, the radial mesh width is adjusted to eliminate the coefficients of the grids at the inner boundary so that there is no inner boundary condition needed. Here, the first radial grid point r_0 is set as $\Delta r/2$ with the radial grid width Δr. The interpolation in the Vlasov solver inside $r_0 = \Delta r/2$ is performed with the mapping from the polar to rectangular coordinates, where the $1/r$ singularity can be avoided in the rectangular coordinate system.[27] With this technique, the theta dependence of the Jacobian is taken into account appropriately in GYSELA as well as in GT5D, except for the linear GYSELA simulations with Neumann boundary condition as described below.

Three different choices for the inner boundary conditions can be used in GYSELA. However, we employ the new boundary condition (called the Null boundary condition hereinafter) for all the simulation shown in this paper except for linear simulations, which is closer to the natural boundary condition at the magnetic axis in GT5D. In the linear simulations, we used the Neumann boundary condition with $\rho_{min} = 0.01$ instead. The use of different boundary conditions can be justified, since the axisymmetric $\phi_{00} = 0$ is filtered out in the linear simulations and is nothing to do with the results. We solve the plasma region $\rho_{min} < \rho < \rho_{max}$, with $\rho_{min} = 0$ (or 0.01 for linear simulations) and $\rho_{max} = 1.0$ for GYSELA and $\rho_{min} = 0$ and $\rho_{max} = 1.0$ for GT5D. Figure 2 shows examples of meshes in GYSELA and GT5D. For simplicity, the low resolution cases with $(N_r, N_\theta) = (16, 32)$ for GYSELA and $(N_R, N_Z) = (16, 16)$ for GT5D are shown here. As is easily seen from Fig. 2(a), the core region is well resolved while the edge region may be under resolved in GYSELA. Figure 2(a) corresponds to the Dirichlet or Neumann boundary condition, and is no longer correct for the Null boundary condition wherein the inner hole disappears.

As summarized in Sec. III E, we choose the resolutions in each code to be the same in the edge region $\rho \sim 0.9$.

D. Normalization

In order to compare the values directly, we employ a common normalization that is different from the ones used in both codes. The normalizations used in this paper are summarized in Table I, where the notation $\hat{X}$ is used for the dimensionless value of X.

The subscripts s represents the species. Here, we employed the reference variables including a reference mass $m_0 = A_0 m_p$, a reference charge $e_0 = Z_0 e$, a reference magnetic field B_0 on magnetic axis and a reference temperature T_0, where m_p is the proton mass. The over-lined value means the value evaluated with the volume averaged density and temperature, and the value without it means the value at the mid-minor radius $\rho(= r/a) = 0.5$.

E. Simulation settings

Since there are many different benchmarking parameters, it appears useful to summarize all relevant physical, geometrical, and numerical settings for the different benchmark cases (neoclassical, zonal flow, linear microinstabilities, nonlinear decaying turbulence and nonlinear flux-driven turbulence).

Tables II and III show the relevant numerical and physical settings used in this paper. The numerical settings are kept the same as in conventional runs in the spirit of presenting the consistency with previous publications. On the other hand, we use the exactly same physical parameters. In the

TABLE I. Comparisons of the normalizations in this work and the original ones in each code.

Common normalization	GYSELA	GT5D
$m_s = m_0 \hat{A}_s$	$m_s = m_0 \hat{A}_s$	$m_s = m_0 \hat{A}_s$
$e_s = Z_0 e \hat{Z}_s$	$e_s = Z_0 e \hat{Z}_s$	$e_s = Z_0 e \hat{Z}_s$
$l = \rho_{t0} \hat{l}$	$l = \rho_{t0} \hat{l}$	$l = \overline{\rho_{t0}} \hat{l}$
$t = \hat{t} R_0 / v_{t0}$	$t = \hat{t} / \Omega_{c0}$	$t = \hat{t} R_0 / \overline{v_{t0}}$
$n_s = n_0 \hat{n}_s$	$n_s = n_0 \hat{n}_s$	$n_s = \overline{n_0} \hat{n}_s$
$T_s = T_0 \hat{T}_s$	$T_s = T_0 \hat{T}_s$	$T_s = \overline{T_0} \hat{T}_s$
$B = B_0 \hat{B}$	$B = B_0 \hat{B}$	$B = B_0 \hat{B}$

TABLE II. Numerical settings for the different benchmarking cases.

GYSELA	$(N_r, N_\theta, N_\varphi, N_{v_\parallel}, N_\mu)$	Wedge size	Inner boundary	Time step	Collision	Source/Sink
Linear	$(256, 256-512, 128-256, 128, 16)$	1	Neumann	10-40	OFF	OFF
Neoclassical	(256, 256, 16, 128, 16)	1/2	Null	10	ON	OFF
Zonal flow	(256, 256, 16, 128, 32)	1	Null	5	OFF	OFF
Nonlinear	(256, 256, 32, 128, 16)	1/6	Null	15	ON	OFF
Flux driven	(256, 256, 32, 128, 16)	1/6	Null	15	ON	ON
GT5D	$(N_R, N_z, N_\varphi, N_{v_\parallel}, N_{v_\perp})$	Wedge size	Boundary	Time step	Collision	Source/Sink
Linear	(200-400, 200-400, 16, 128, 16)	1/5–1/30	Natural	5-10	OFF	OFF
Neoclassical	(200, 200, 1, 128, 16)	1	Natural	5	ON	OFF
Zonal flow	(200, 200, 1, 128, 32)	1	Natural	5	OFF	OFF
Nonlinear	(200, 200, 32, 128, 16)	1/6	Natural	5	ON	OFF
Flux driven	(200, 200, 32, 128, 16)	1/6	Natural	5	ON	ON

linear simulations, we increased the perpendicular grid resolutions and decreased the time step size for $n=25$ and 30 cases in both codes. Correspondingly, we increased the resolution in toroidal direction in GYSELA while keeping the wedge size. In contrast, we reduced the wedge size while keeping the resolution in toroidal direction in GT5D.

IV. BENCHMARKS OF COLLISIONAL TRANSPORT AND ZONAL FLOW DYNAMICS

Let us begin with the benchmarking of collisional transport and poloidal flow dynamics, namely, neoclassical transport in the axisymmetric limit and zonal flow dynamics. The neoclassical results can be obtained at the drift kinetic limits as shown in Ref. 17.

A. Neoclassical benchmarks

As for the neoclassical benchmarks, we compare the neoclassical ion heat flux and the parallel flow relation at a quasi-equilibrium state. The grid points used in GYSELA and GT5D are $(N_r, N_\theta, N_\varphi, N_{v_\parallel}, N_\mu) = (256, 256, 16, 128, 16)$ and $(N_R, N_z, N_\varphi, N_{v_\parallel}, N_{v_\perp}) = (200, 200, 1, 128, 16)$, respectively. The $\rho_*^{-1} \equiv a/\rho_{\rm ti} = 150$ is employed here, which is carefully chosen to be equivalent for both codes (see the normalization defined in Sec. III D). The profiles used in this neoclassical computation are shown in Fig. 3. As explained in Sec. III D, the normalized variables like $v_{\rm ti}$, ρ_{ti}, and T_i are the ones defined at the mid-minor radius at $t=0$ in the following.

The temperature and density gradients are set identical, that is, $\eta_i = L_{\rm ti}/L_n = 1$, wherein the ITG mode is stable. In addition, we consider the plasma with large aspect-ratio with $\epsilon_a^{-1} = R_0/a = 1.738/0.3477 = 5$, in order to mimic the large aspect ratio assumption used in the neoclassical theory. Here, ϵ_a represents the inverse aspect ratio. In this configuration, we can focus on the neoclassical dynamics (without turbulence) and direct comparisons against neoclassical theory are possible. The low resolution in the toroidal direction reflects the axisymmetrical nature of this test.

TABLE III. Physical parameters at the mid-minor radius $\rho = 0.5$ for the different benchmarking cases.

	$R_0/L_{\rm ti}$	$R_0/L_{\rm n}$	$\tau = T_i/T_e$	ν_*	ϵ	q	$\hat{s}$
Linear	6.92	2.22	1.0	0	0.18	1.4	0.78
Neoclassical	6.0	6.0	1.0	0.01-10	0.1	1.4	0.78
Zonal flow	10^{-7}	10^{-7}	1.0	0.18	1.4	0	0
Nonlinear	6.92	2.22	1.0	0.02	0.18	1.4	0.78
Flux driven	10.0	2.22	1.0	0.02	0.18	1.4	0.78

For the collisionality dependency of the ion thermal diffusivity, we use a well-known formula derived by Chang-Hinton[28]

$$\chi_i/\chi_{i,\rm GB} = 2\sqrt{2}\nu_* K_2,$$
$$K_2 = \left(\frac{0.66 + 1.88\epsilon^{1/2} - 1.54\epsilon}{1 + 1.03\nu_*^{1/2} + 0.31\nu_*}\right)\left\langle\frac{B_0^2}{B^2}\right\rangle_f + \frac{0.79}{\epsilon^{1/2}}\left(\frac{0.74\nu_*\epsilon^{3/2}}{1 + 0.74\nu_*\epsilon^{3/2}}\right)\left[\left\langle\frac{B_0^2}{B^2}\right\rangle_f - \left\langle\frac{B^2}{B_0^2}\right\rangle_f^{-1}\right], \tag{17}$$

with the gyro-Bohm coefficient $\chi_{i,\rm GB} = \rho_{\rm ti}^2 v_{\rm ti}/R_0$ and $\epsilon = r/R_0$. The factor $2\sqrt{2}$ results from our definition of the thermal velocity $v_{\rm ti} = \sqrt{T_i/m}$, whereas Chang-Hinton uses $v_{\rm Ti} = \sqrt{2T_i/m}$. The effective collision frequency is given by $\nu_* = qR_0/(\epsilon^{3/2}\tau_{ii}v_{\rm ti})$. Figure 4 shows the collisionality dependence and its comparison with Chang-Hinton's theory. The neoclassical ion heat diffusivity $\chi_i^{\rm Neo} = -Q_i^{\rm Neo}/(n_i\nabla T_i)$ is defined using the heat flux driven by the curvature drift

$$Q_i^{\rm Neo} \equiv \left\langle \int d^3\mathbf{v} f \mathbf{v}_D \cdot \nabla r \right\rangle_f. \tag{18}$$

Concerning experimentally relevant plasmas where the collisionality ν_* varies a lot in the radial direction, it is quite important to verify the applicability of the codes for a wide range of ν_*. We found good agreement for a wide range of ν_*, namely, banana and plateau regimes as shown in Fig. 4.

From the first order gyrokinetic theory, the radial force balance equation can be derived

$$\frac{e_i E_r}{T_i} = \frac{m_i\Omega_i}{T_i R B_t}\frac{d\psi}{dr}\langle U_\parallel\rangle_f + \frac{d\ln\langle n_i\rangle_f}{dr} + \left[1 - k(\nu_*,\epsilon)\right]\frac{d\ln\langle T_i\rangle_f}{dr}, \tag{19}$$

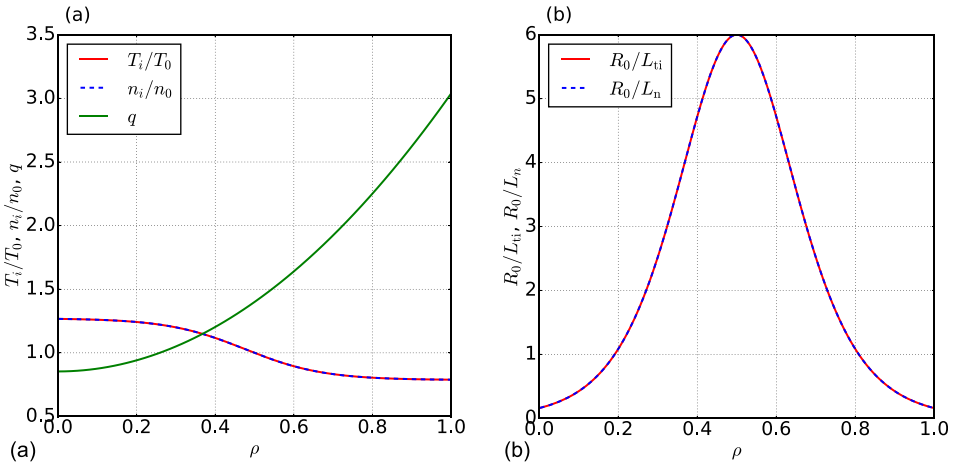

FIG. 3. (a) Initial radial profiles of density, temperature, safety factor, and (b) temperature and density gradients used for neoclassical benchmarks.

where E_r is the radial electric field, $U_\parallel$ the parallel mean flow velocity, $R = R_0 + r\cos\theta$ is the plasma major radius, B_t the toroidal magnetic field, and ψ the poloidal flux. The coefficient k is a coefficient of the neoclassical poloidal flow. Based on Hinton's theory,[29] the coefficient (the H-H formula) is

$$k(\nu_*, \epsilon) = \left(\frac{1.17 - 0.35\nu_*^{1/2}}{1 + 0.7\nu_*^{1/2}} - 2.1\nu_*^2\epsilon^3\right) \Big/ \left(1 + \nu_*^2\epsilon^3\right). \quad (20)$$

Similar to Ref. 16, we compare the radial profile of the electric field against the theoretical estimate. Since neoclassical theory gives an estimate of the poloidal flow, we can estimate the radial electric field based on the radial force balance equation Eq. (19). Figure 5 shows the radial electric field computed from the electrostatic potential and from Eq. (19) for $\nu_* = 0.1$ case. We drew two theoretical estimates using profiles from GYSELA and GT5D, respectively. The time evolution of profiles is very close with each other but not exactly the same, especially when looking at the derivatives like temperature gradients. We found good agreements with the H-H formula in both codes, confirming that the collision operators in both codes produce the appropriate neoclassical poloidal flows.

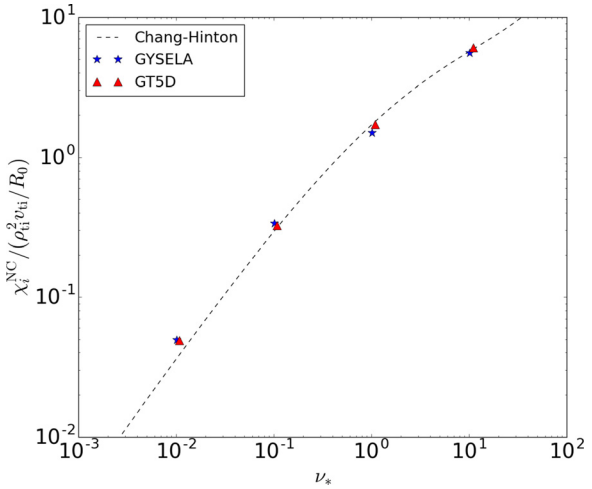

FIG. 4. The collisionality dependence of the ion heat diffusivity χ_i with the radial average for $r/a = 0.4 - 0.6$. The dashed curve shows the analytical estimation by Chang-Hinton's formula.

B. Zonal flow dynamics

In the collisionless regime, the dynamics of the zonal component ϕ_{00} can be calculated analytically.[30,31] Namely, the time oscillatory components or geodesic acoustic modes (GAMs) are decaying towards the residual poloidal flow. In this section, we computed the time evolution of zonal flow component ϕ_{00} and compared its damping rate and residual level against theory. The initial distribution function is given by $f = f_{eq}(1 + \varepsilon\sin(2\pi(r/2a)))$ with a perturbation amplitude $\varepsilon = 10^{-5}$. As shown in the work by Sugama and Watanabe, the time evolution of the zonal-flow potential is given by

$$\phi_{00}(t) = \phi_{00}(\infty) + \left[\phi_{00}(0) - \phi_{00}(\infty)\right]\cos(\omega_G t)\exp(\gamma t), \quad (21)$$

where $\phi_{00}(\infty) = \phi_{00}(0)/(1 + 1.6q^2/\epsilon^{1/2})$ is the residual zonal flow derived by Rosenbluth-Hinton.[30] ω_G and γ are the frequency and damping rate of GAM. Since the analytical theories[30,31] are derived in the local limit, we employ radially uniform profiles to eliminate global effects. The safety

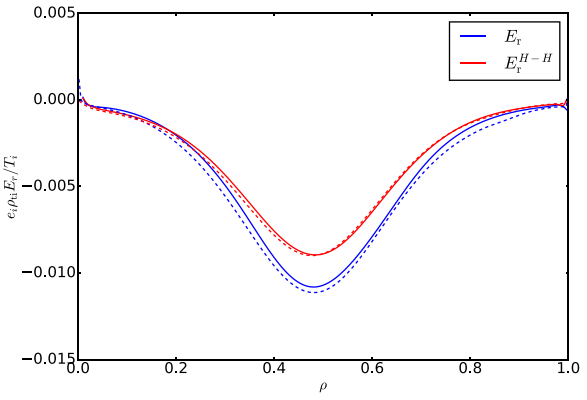

FIG. 5. Radial profile of electric field E_r against the theoretical estimate E_r^{H-H} at $tR_0/v_{ti} = 130$ from GYSELA and GT5D. Solid lines correspond to GYSELA results and dashed lines correspond to GT5D results. Theoretical values E_r^{H-H} are estimated using the profiles of GYSELA and GT5D, respectively.

factor profile is given by $q(\rho) = 1.5\ (\forall \rho \in [0,1])$, and the aspect ratio is set as $\epsilon_a = a/R_0 = 0.18$. The density and temperature profiles are almost constant with $R_0/L_{T_i} = R_0/L_n = 10^{-7}$. The grid points used in GYSELA and GT5D are $(N_r, N_\theta, N_\varphi, N_{v_\parallel}, N_\mu) = (256, 256, 16, 128, 32)$ and $(N_R, N_z, N_\varphi, N_{v_\parallel}, N_{v_\perp}) = (200, 200, 1, 128, 32)$, respectively. The $\rho_*^{-1} = 150$ is used here.

Figure 6 shows the time evolution of ϕ_{00} mode at $\rho = 0.5$ and corresponding analytical results. They show good agreements with the theoretical estimates of frequencies, damping rates, and residual flow levels. Table IV shows the estimates of frequencies and damping rates from simulations and theories. From simulations, the GAM frequency is estimated by FFT with the time window of $0 \le tR_0/v_{\rm ti} \le 50$, and the damping rate is estimated for the time window of $10 \le tR_0/v_{\rm ti} \le 20$. The shorter time window for the damping rate estimate is chosen to avoid the time-evolution of the radial wavenumber k_r of ϕ_{00} mode.

For the wavenumber used to estimate the damping rate analytically, we employed the same initial radial wavenumber of ϕ_{00} mode, that is, $k_r\rho_{\rm Ti} = (2\pi/2a) \times \sqrt{2}\rho_{\rm ti} = \sqrt{2}\pi\rho_* = 0.0296$.

Difficulty of this benchmark lies in the time-evolution of k_r, which is largely affected by boundary conditions. As described in Eq. (2.10) in Ref. 31, the damping rate of GAM depends on k_r. Thus, it is important to give the appropriate boundary conditions for two codes. In addition, it would be helpful to investigate the point near the mid-minor radius $\rho = 0.5$, in order to minimize the influence from the boundaries.

V. BENCHMARKS OF MICROINSTABILITY

To benchmark microinstability, we considered the Cyclone-Base case (CBC),[2] which is a standard benchmark case for local δf gyrokinetic simulations. Contrary to the local δf gyrokinetic simulations, we have to take into account

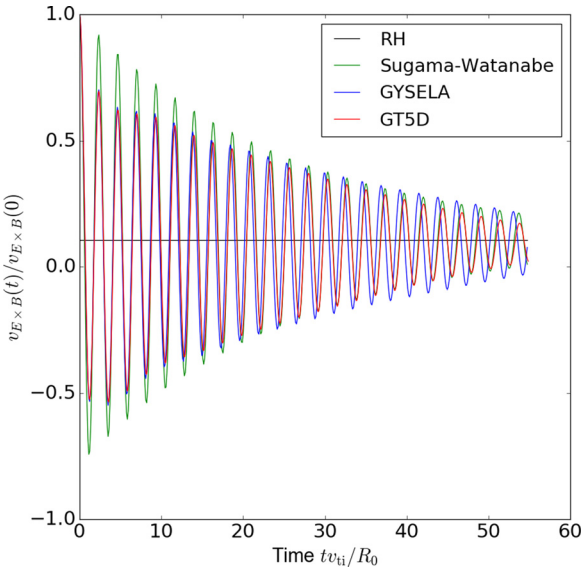

FIG. 6. The time evolution of the normalized $E \times B$ flows in Rosenbluth-Hinton test. The residual value is compared with Rosenbluth-Hinton theory. The GAM frequencies and damping rates are compared with theoretical predictions by Sugama and Watanabe.

TABLE IV. Estimates of frequencies and damping rates from simulations and the theories.[30,31]

	$\gamma R_0/v_{\rm ti}$	$\omega_G R_0/v_{\rm ti}$
GYSELA	−0.031	2.644
GT5D	−0.036	2.643
Sugama-Watanabe	−0.039	2.690

the plasma profiles. The initial plasma distribution function is given by a local Maxwellian. The density n_i, temperature T_i, safety factor q, and the magnetic field $\mathbf{B}$ are given by the following form:

$$n_i(\rho) = n_0 \exp\left[-\frac{\Delta_n}{L_n}\tanh\left(\frac{\rho - 0.5}{\Delta_n/a}\right)\right], \tag{22}$$

$$T_i(\rho) = T_{i0} \exp\left[-\frac{\Delta_{Ti}}{L_{Ti}}\tanh\left(\frac{\rho - 0.5}{\Delta_{Ti}/a}\right)\right], \tag{23}$$

$$q(\rho) = 0.854 + 2.184\rho^2, \tag{24}$$

$$\mathbf{B} = \frac{B_0 R_0}{R}\left[\frac{r}{qR_0}\mathbf{e}_\theta + \mathbf{e}_\varphi\right], \tag{25}$$

where $\rho = r/a$ is the normalized minor radius, B_0 is the magnetic field at the magnetic axis, and $\mathbf{e}_\theta$ and $\mathbf{e}_\varphi$ are poloidal and toroidal unit vectors. We choose $\Delta_n/a = 0.3$ and $\Delta_{T_i}/a = 0.3$ for density and temperature profiles. Figure 7 shows the initial radial profile of ion temperature T_i, density n_i, and safety factor q.

The electron and ion temperature profiles are the same so that $\tau = T_i/T_e = 1$ everywhere. At the mid-minor radius $\rho = 0.5$, the profile gives the CBC parameters as $R_0/L_{Ti} = 6.92$, $R_0/L_n = 2.22$, $\tau = T_i/T_e = 1.0$, $q = 1.4$, and $\hat{s} = 0.78$. Although the normalized Larmor radius for original DIII-D shot 81499[32] is given by $\rho_*^{-1} = 180$ with $R = 1.71$ m and $a = 0.625$ m, we consider $\rho_*^{-1} = 150$ with $R = 1.01$ m and $a = 0.365$ m to reduce the computational costs.

A. Linear benchmarks

As for linear benchmarks, we compared the linear growth rate and real frequency of ITG modes. As discussed in Ref. 13, the separation between linear and non-linear terms is not possible in a full-F code. In order to avoid the coupling of different toroidal modes, we filtered out all the toroidal modes except the initial one. The filtering is performed just after solving the quasi-neutrality equation. For example, Fig. 8 contains 6 different linear simulations initialized with $n = 5, 10, 15, 20, 25, 30$. The corresponding poloidal mode number is computed by using the relationship $k_\theta\rho_{\rm ti} = nq_0\rho_* a/r_0$ with $r_0 = a/2$ and $q_0 = q(r_0)$. Since the high toroidal mode number is equivalent to a tiny structure both in toroidal and poloidal directions, we doubled the numbers of grid points both in toroidal and poloidal directions for the simulations with $n \ge 25$.

Figure 8 shows the linear growth rate and real frequency of ITG mode computed at the mid-minor radius $\rho = 0.5$ from 6 different runs. Both the linear growth rate and real frequency show quantitative agreements between GYSELA and GT5D.

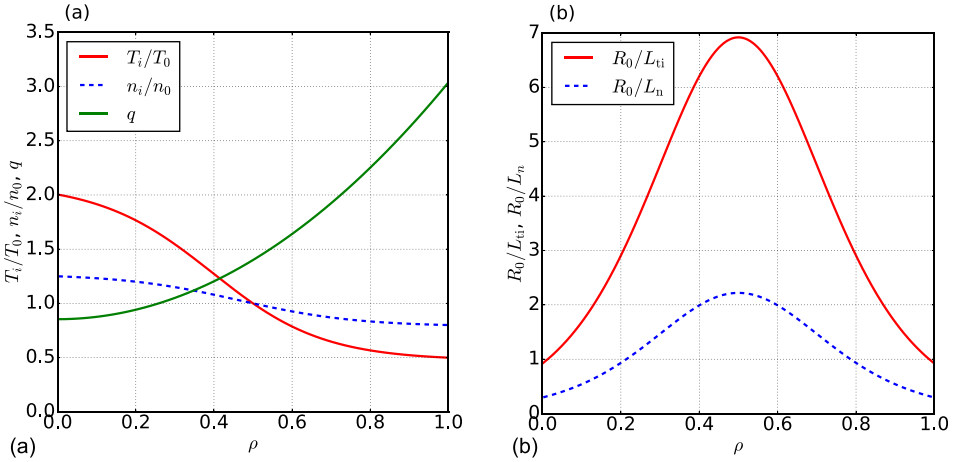

FIG. 7. (a) Initial radial profiles of density, temperature, safety factor, and (b) temperature and density gradients based on Cyclone-base case.

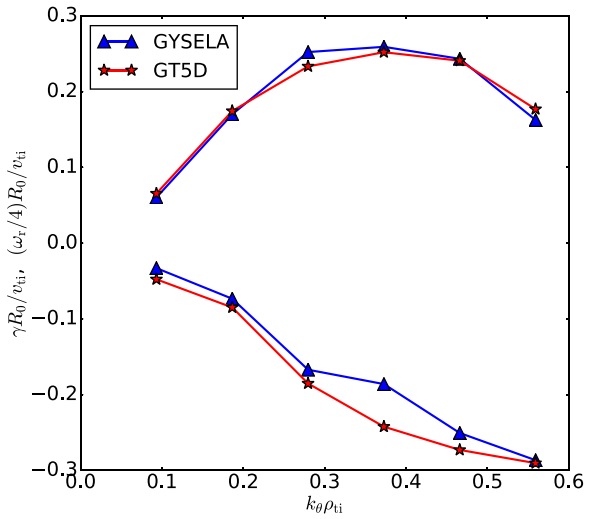

FIG. 8. Linear growth rate and real frequency obtained by GYSELA (blue) and GT5D (red).

The global structures of the linear eigenmodes have also been compared. Figure 9 shows the global mode structure of the linear eigenmode with $n = 15$. A similar shape of global eigenmode is found, including the radial peak position and the ballooning angle.

B. Nonlinear decaying turbulence

In this section, we present the benchmarks for nonlinear decaying turbulence, i.e., without sink and source terms. Weak collision with $\nu_* \sim 0.01$ is added in order to avoid unphysical solution coming from the absence of diffusion in the $v_\parallel$ direction. In the collisionless limit, the fine structures in the $v_\parallel$ direction generated by parallel phase mixing will reach the grid scale at a recurrence time. Therefore, the solution will be unphysical after the recurrence time in the collisionless limit.

The initial condition is given by

$$\bar{F}_s = \bar{F}_{s,\rm eq}\left(1 + \varepsilon \sum_{n=1}^{n_{\max}} \sum_{m=m_{\min}(n)}^{m_{\max}(n)} \cos\left(m\theta + n\varphi + \delta_{mn}\right)\right), \tag{26}$$

where $m_{\min}(n) = \max[1, nq - \delta m]$ and $m_{\max}(n) = \min[m_{\max}, nq + \delta m]$, with $n_{\max} = 18$, $m_{\max} = 70$, and $\delta m = 8$. The perturbed amplitude is set as $\varepsilon = 10^{-6}$. Since the decaying turbulence simulations are sensitive to initial conditions, we use exactly the same initial conditions for the two codes. The grid points used in GYSELA and GT5D are $(N_r, N_\theta, N_\varphi, N_{v_\parallel}, N_\mu) = (256, 256, 32, 128, 16)$ and $(N_R, N_z, N_\varphi, N_{v_\parallel}, N_{v_\perp}) = (200, 200, 32, 128, 16)$, respectively. In order to save the computational cost, we employed one sixth of a torus based on convergence tests.[33] The time step size is set as $\Delta t \Omega_i = 15$ in GYSELA and 5 in GT5D.

The time evolution of the turbulent heat diffusivity χ_i and the normalized temperature gradient $R_0/L_{\rm ti}$ is plotted in Fig. 10. The turbulent ion heat diffusivity $\chi_i = -Q_i/(n_i \nabla T_i)$ is defined using the heat flux driven by $E \times B$ drift velocity

$$Q_i^{\rm Turb} \equiv \left\langle \int d^3\mathbf{v} f \mathbf{v}_{E\times B} \cdot \nabla r \right\rangle_f. \tag{27}$$

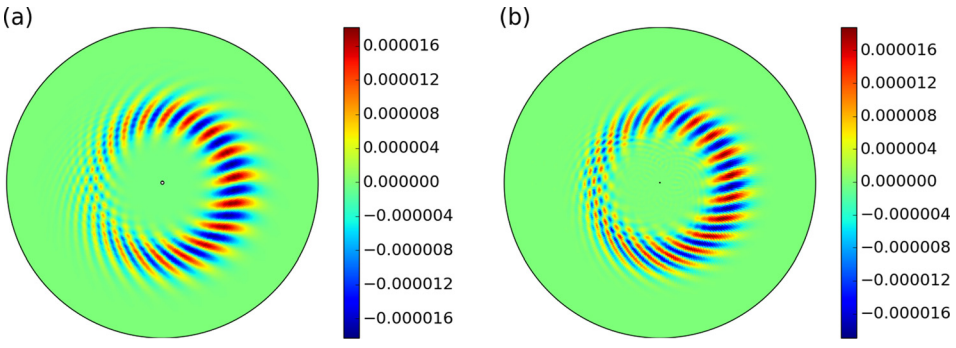

FIG. 9. Linear eigen functions of the most unstable mode with $n = 15$ obtained by (a) GYSELA and (b) GT5D.

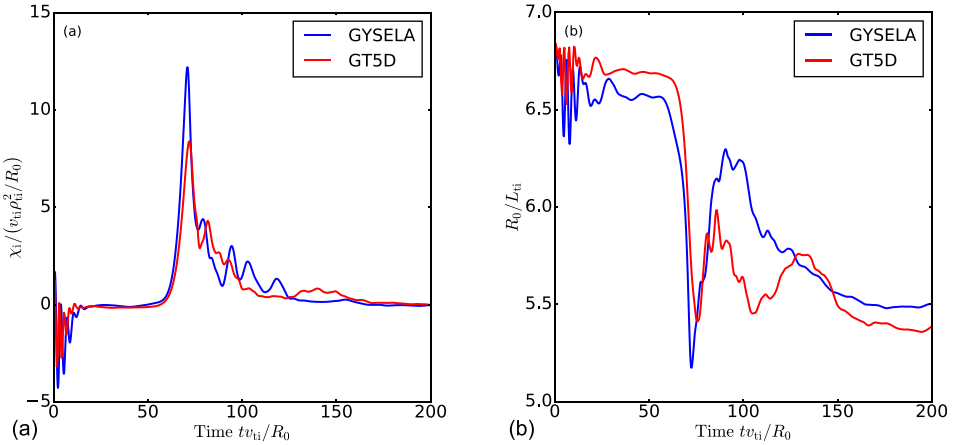

FIG. 10. Time evolution of the turbulent heat diffusivity χ_i (a) and normalized ion temperature gradient R_0/L_{ti} (b) averaged for $0.45 \leq \rho \leq 0.55$. The heat flux level converges to the same nonlinear critical gradient $R_0/L_{ti} \sim 5.5$, where the ion heat transport is almost quenched.

As shown in Fig. 10(a), the time scale for the initial transient and final steady phase shows good agreements in GYSELA and GT5D. Although the initial saturation level is not exactly the same, the asymptotic state transport levels are close to zero in both codes, implying that turbulence is almost quenched. Because of the chaotic nature of plasma turbulence, a perfect agreement in time evolution cannot be expected after the initial transient phase, that is, the turbulent phase. Thus, we compare well-defined properties like the critical temperature gradient and the relaxation process toward the asymptotic state. The steady state temperature gradients are $R_0/L_{ti} \sim 5.5$ in Fig. 10(b), which is consistent with the effective critical gradients found in Ref. 2. The nonlinear threshold value is confirmed from Fig. 11, which shows the temperature gradient and turbulent transport values at successive time points during profile relaxation. Both codes show a relaxation toward the temperature gradient $R_0/L_{ti} \sim 5.5$, where the turbulent transport is almost quenched. Figure 12 shows the time evolution of the root mean square of the electrostatic potential $e_i\phi/T_i$, where zonal components, GAM components and other contributions are separately plotted. Here, we found that the time evolutions of zonal components are roughly the same and dominate turbulence in the asymptotic state. We can also confirm that the behavior of the turbulent components are quite similar, both in the linear phase with $50 \leq tv_{ti}/R_0 \leq 70$ and the asymptotic state phase with $tv_{ti}/R_0 \geq 160$.

Figure 13 shows contours of the $n \neq 0$ components of the electrostatic potential $e_i\phi/T_i$ in the decaying phase. The amplitude of the normalized potential is about $e_i\phi/T_i \sim 0.03$ for both codes. Since the formation of the mean electric field has a large impact on transport properties, we analyzed the spatio-temporal evolutions of the radial electric field E_r and turbulent ion heat flux χ_i^{turb} as shown in Fig. 14. As expected, the heat transport is quenched almost everywhere in both codes after $tv_{ti}/R_0 \geq 160$. The quench of turbulent heat transport is presumably the consequence of the turbulence regularization by the radial electric field shear found in Figs. 14(c) and 14(f). The temperature gradient is kept almost constant with $R_0/L_{ti} \sim 5.5$ after the initial transient phase [see Figs. 14(b) and 14(e)].

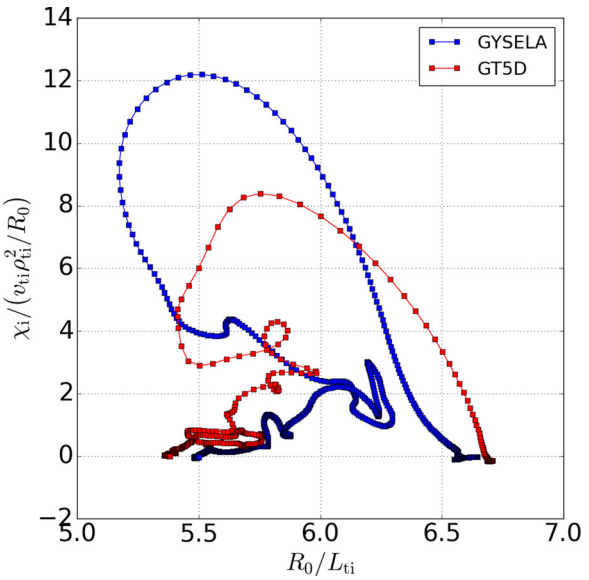

FIG. 11. Time evolution of the turbulent heat diffusivity χ_i and normalized ion temperature gradient R_0/L_{ti} averaged for $0.45 \leq \rho \leq 0.55$. The heat flux level converges to the same nonlinear critical gradient $R_0/L_{ti} \sim 5.5$, where the ion heat transport is almost quenched.

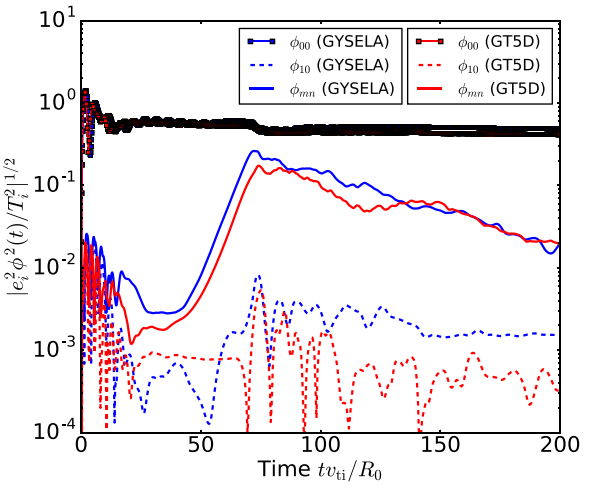

FIG. 12. Time evolutions of the root mean square of the electrostatic potential $e_i\phi/T_i$ at the mid-minor radius $\rho = 0.5$. The zonal component $\phi_{0,0}$ is represented by the line with squares, the GAM component $\phi_{1,0}$ is represented by the dotted line and the summation of other modes $\sum_{m,n} \phi_{m,n}$ are plotted with lines.

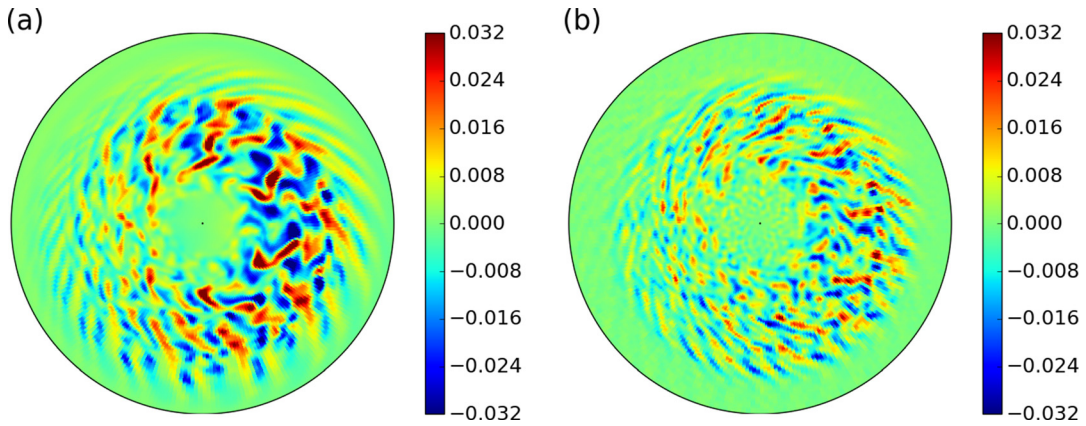

FIG. 13. Contours for $n \neq 0$ components of the electrostatic potential at $tv_{\mathrm{ti}}/R_0 = 100$ from (a) GYSELA and (b) GT5D.

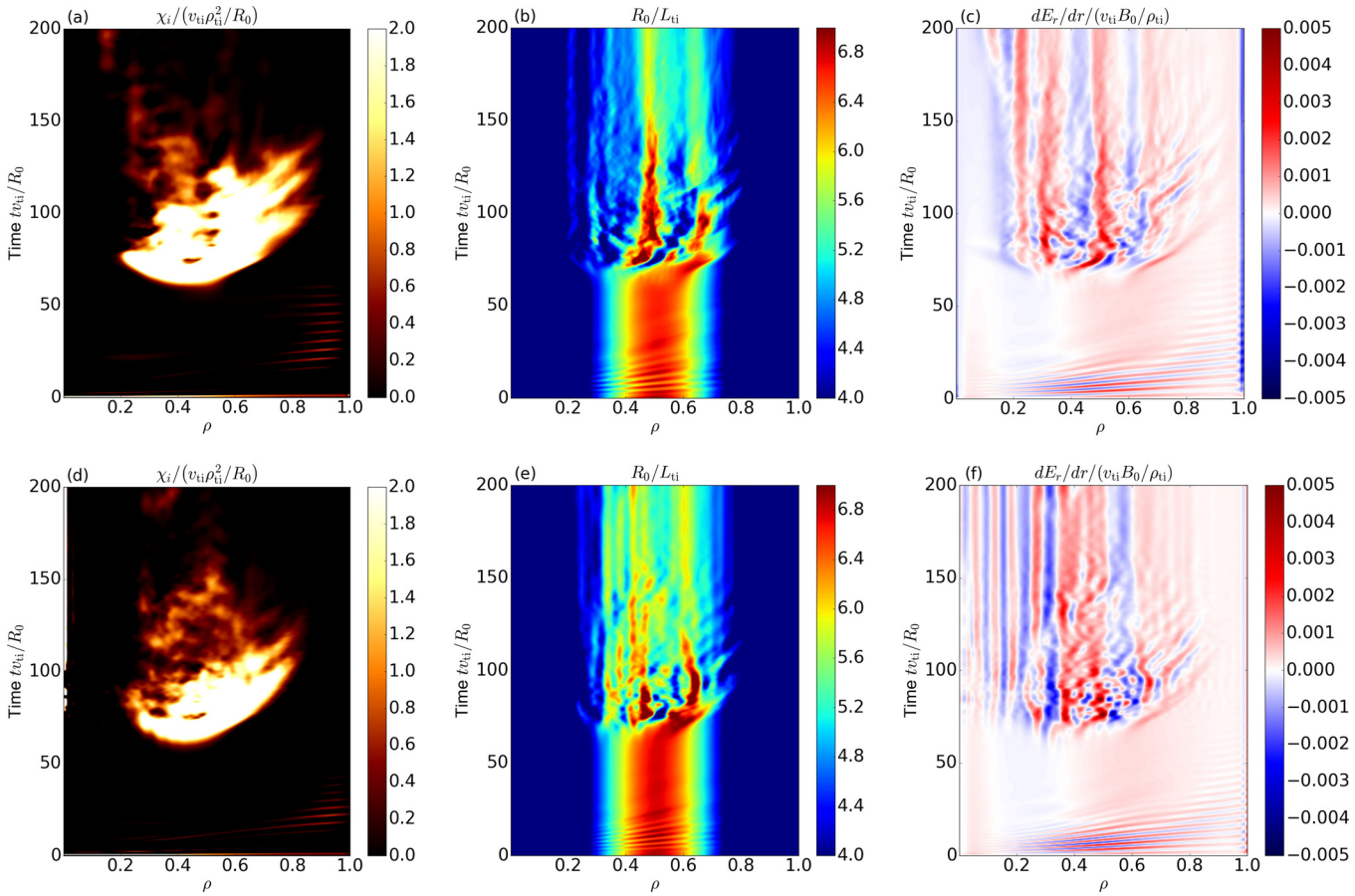

FIG. 14. Spatio-temporal evolutions of the ion turbulent heat diffusivity $\chi_i/(\rho_{\mathrm{ti}}^2 v_{\mathrm{ti}}/R_0)$ [(a) and (d)], the normalized temperature gradient R_0/L_{ti} [(b) and (e)] and the radial electric field shear dE_r/dr [(c) and (f)] in GYSELA (upper row) and GT5D (lower row).

In order to compare the global mode structure quantitatively, we computed the radial and time correlation functions of electrostatic potential fluctuations $\tilde{\phi} = \phi - \phi_{n=0}$. We employed the following definition for the correlation function:

$$C_\phi(t_{\mathrm{lag}}, r_{\mathrm{lag}}) = \frac{\int dt \int dr \langle \tilde{\phi}\left(t + t_{\mathrm{lag}}, r + r_{\mathrm{lag}}, \varphi, \theta = 0\right) \tilde{\phi}(t, r, \varphi, \theta = 0) \rangle_\varphi}{\int dt \int dr \langle \tilde{\phi}^2(t, r, \varphi, \theta = 0) \rangle_\varphi}, \tag{28}$$

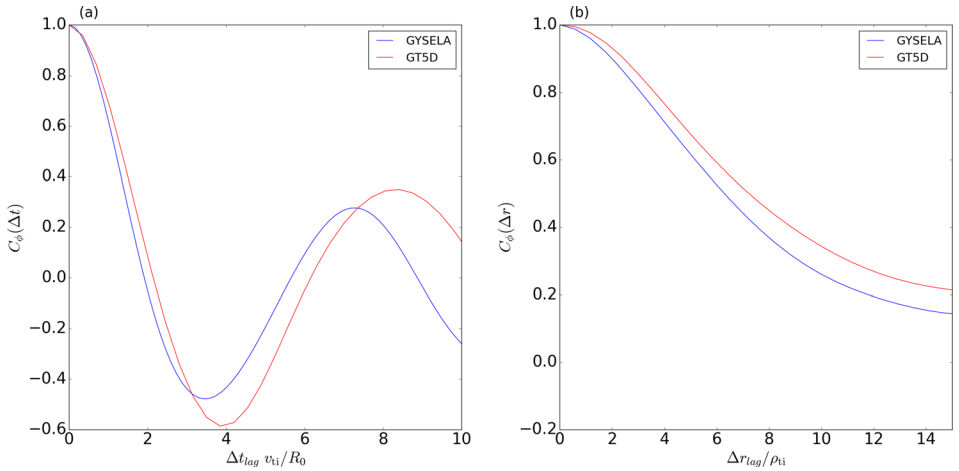

FIG. 15. (a) Temporal and (b) radial self-correlation functions computed from $n \neq 0$ components of electrostatic potential $e_i\phi/T_i$ for GYSELA and GT5D, during the time period of $tv_{ti}/R_0 = 160 - 180$.

where $\langle\rangle_\varphi$ stands for the average in toroidal angle φ. As shown in Fig. 15, both codes show the quite similar correlation length around $\Delta r_{lag}/\rho_{ti} \sim 6$ and correlation time around $\Delta t_{lag} v_{ti}/R_0 \sim 2$.

VI. BENCHMARKS FOR FLUX DRIVEN SIMULATIONS

In the flux driven simulations, we employ basically the same physical parameters as for decaying turbulence simulation except for a larger temperature gradient, $R_0/L_{ti} = 10$ at the mid minor radius $\rho = 0.5$. The input power is set to 2MW, whose radial and velocity space profiles are given in Sec. II C. The Krook-type sink operator is applied in the buffer region near the edge as described in Sec. II D. The grid points used in GYSELA and GT5D are $(N_r, N_\theta, N_\varphi, N_{v_\parallel}, N_\mu) = (256, 256, 32, 128, 16)$ and $(N_R, N_z, N_\varphi, N_{v_\parallel}, N_{v_\perp}) = (200, 200, 32, 128, 16)$, respectively. As well as the nonlinear decaying turbulence case, we employed the one sixth wedge torus model. The time step size is set as $\Delta t\Omega_i = 10$ in GYSELA and 5 in GT5D. The gradient of initial ion temperature profile $R_0/L_{ti} = 10$ is above the linear and nonlinear thresholds with $R_0/L_{ti} \sim 4.5$ and $R_0/L_{ti} \sim 6.0$, respectively. The nonlinear threshold value can be identified from Fig. 11, where both GYSELA and GT5D show similar values, namely, $R_0/L_{ti} \sim 5.5$. In this section, we plot the turbulent ion heat flux Q_i rather than the heat diffusivity χ_i in order to differentiate the time evolution of turbulent transport and temperature gradient. As found in Eq. (27), a heat diffusivity χ_i is affected by both heat flux Q_i and temperature gradient R_0/L_{ti}. In flux driven simulations, these quantities evolve self-consistently and exhibit avalanche-like properties. In addition, the time-averaged temperature profile spontaneously corrugates leading to zonal flows and the interplay between zonal flows and avalanches gives rise to the so-called $E \times B$ staircase.[4,5,34,35]

Figure 16 shows the spatio-temporal evolutions of the ion heat flux Q_i, the normalized ion temperature gradient R_0/L_{ti} and the radial electric field shear dE_r/dr. In a source free region ($\rho = 0.5$–0.9), the turbulent heat transport shows the avalanche-like feature in both codes [see Figs. 16(a) and 16(d)]. Correspondingly, the ion temperature gradient profile in Figs. 16(b) and 16(e) exhibits the near threshold value around $R_0/L_{ti} \sim 6$. As found in the time evolution of heat diffusivity [Figs. 16(a) and 16(d)] and radial electric field shear [Figs. 16(c) and 16(f)], there are inward and outward avalanches depending on the sign of the electric field shear. In the positive shear region with $\rho > 0.6$ avalanches propagate outward, while they propagate inward in the negative shear region with $\rho < 0.6$. Both codes agree well on the directions of avalanche propagation and their relationship with the radial electric field shear. Several discussions on this issue are found in Refs. 16, 36, and 37.

Figure 17 shows (a) the steady state profile of the turbulent ion heat flux $Q_i/[n_i T_i v_{ti} \rho_{ti}^2/a^2]$, (b) the normalized ion temperature gradient R_0/L_{ti}, (c) the radial electric field $e_i R_0 E_r/T_i$, and (d) the parallel flow velocity $U_\parallel/v_{ti}$. The time average is taken over $tv_{ti}/R_0 = 300$–750. First of all, we find quite similar radial profiles of the turbulent heat flux. Although there are some differences in the inner region with $0 \leq \rho \leq 0.5$, the temperature gradient in this region is close to the marginal state [Fig. 17(b)] where the transport level should be very sensitive to the temperature gradient. In the marginal state, it has been often reported[5,34] that the temperature gradient profile, poloidal flow profile, and heat transport interplay via meso-scale structure organization. In this regime, a difference in the temperature gradient profile corrugations easily propagates to a transport level. Another important aspect is that the temperature gradient is kept almost constant in this region, which is close to the critical gradient level with $R_0/L_{ti} \sim 6$. The constrained profiles by the nonlinear threshold as in Fig. 17(b) and the staircase meso-scale organization are important characteristics of full-F simulations. As shown in Fig. 17(c), the radial electric field determined by radial force balance shows a global V-shape with a negative peak around the mid minor radius which is consistent with the discussions in Ref. 16. The radial electric field then determines the directions for avalanche propagation. The parallel flow velocity $U_\parallel$ in Fig. 17(d) represents the intrinsic rotation. Although the levels of rotation speeds are not exactly the same, both codes show co-rotation in the core region with $\rho = r/a \sim 0.2$ and counter-rotation in the outer region with $0.5 \leq \rho \leq 1.0$. The larger difference in the core region could be explained by the difference in the inner boundary condition, the Null (resp. natural) boundary condition in GYSELA (resp. GT5D). Another important difference is the source term, where GYSELA imposes the

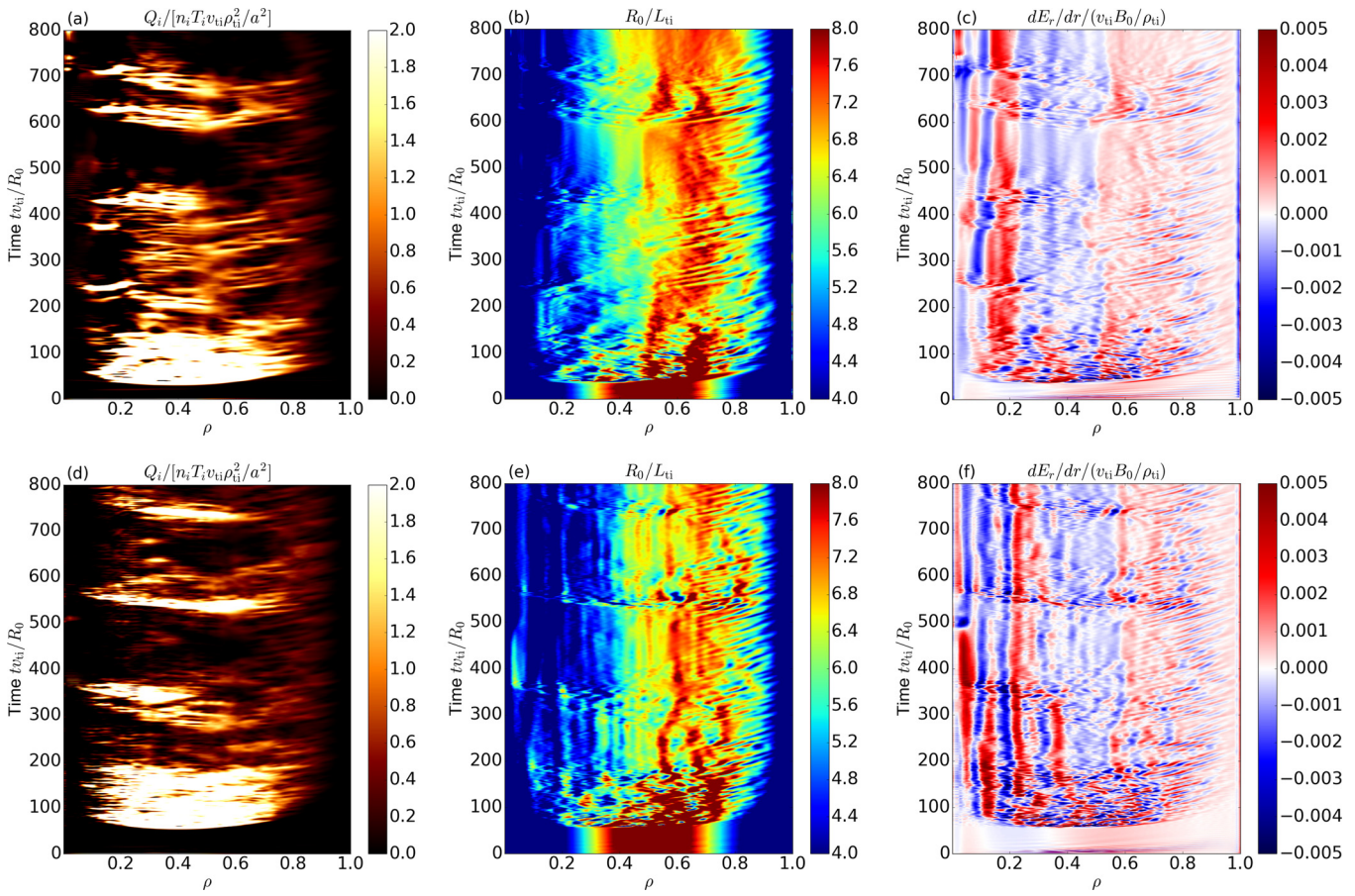

FIG. 16. Spatio-temporal evolutions of the ion turbulent heat flux $Q_i/[n_iT_iv_{ti}\rho_{ti}^2/a^2]$ [(a) and (d)], the normalized temperature gradient R_0/L_{ti} [(b) and (e)] and the radial electric field shear $dE_r/dr/(v_{ti}B_0/\rho_{ti})$ [(c) and (f)] in GYSELA (upper row) and GT5D (lower row).

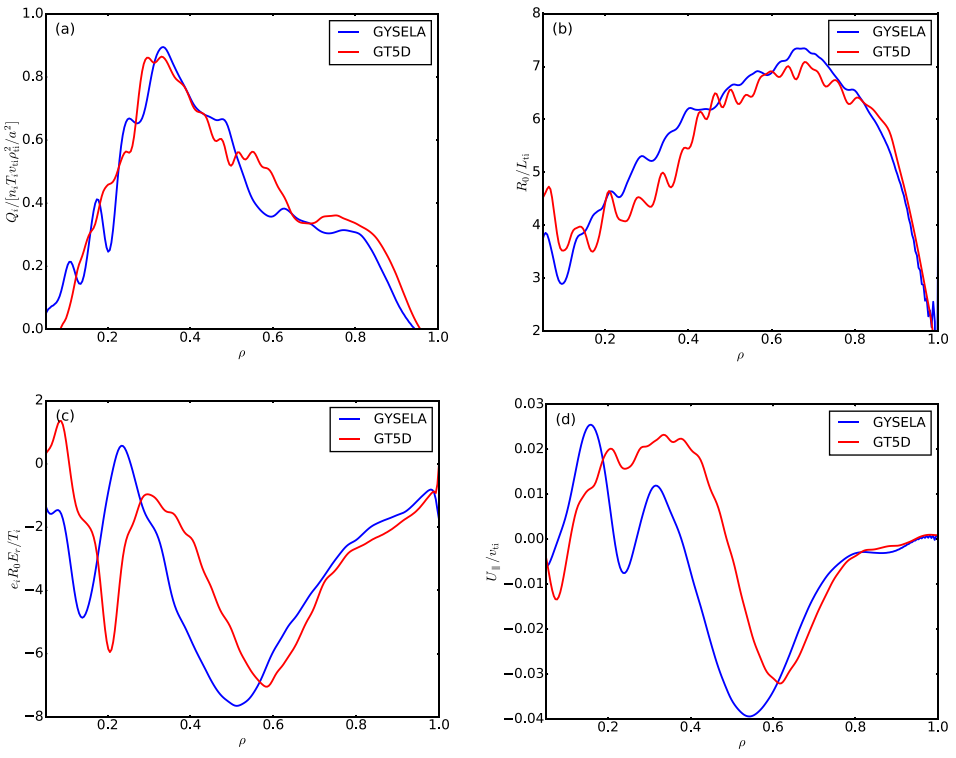

FIG. 17. The quasi-steady state radial profiles (time average over $tv_{ti}/R_0 = 300$–750) of (a) the ion energy flux Q_i, (b) the normalized ion temperature gradient R_0/L_{ti}, (c) the radial electric field E_r, and (d) the parallel flow velocity $U_\parallel$.

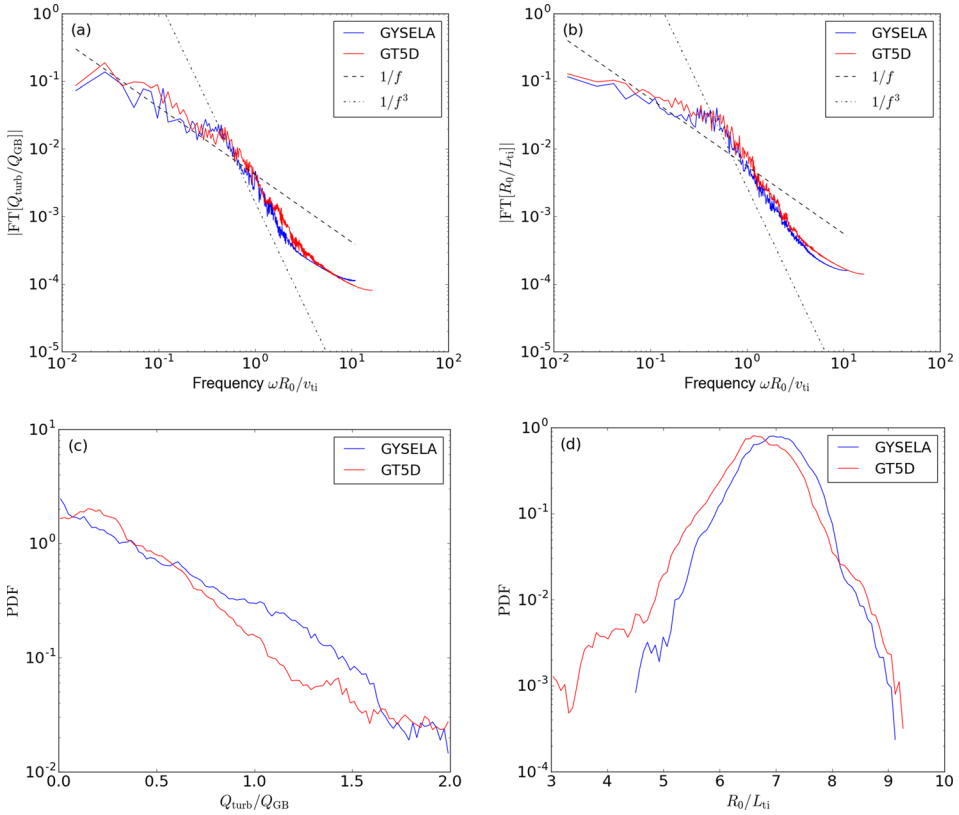

FIG. 18. The statistical analysis of the turbulent heat flux Q_i and R_0/L_{ti} which are evaluated for $300 \leq tv_{\mathrm{ti}}/R_0 \leq 750$ with radial average in source free region ($0.5 \leq \rho \leq 0.8$). The frequency spectra of (a) Q_i and (b) R_0/L_{ti}, and the probability density function (PDF) of (c) Q_i and (d) R_0/L_{ti} are shown.

momentum input in addition to the energy input (see discussions in Sec. II C for detail). It should also be noted that the higher resolution of GYSELA near core could have some impacts (the differences in the boundaries are detailed in Sec. III C). In the consequence, the net rotation, $U_{\parallel,net} = \int drrU_{\parallel} / \int drr$, is slightly different, where GYSELA gives a large negative net rotation $U_{\parallel,net}/v_{\mathrm{ti}} \sim -0.0069$ and GT5D gives a small negative net rotation $U_{\parallel,net}/v_{\mathrm{ti}} \sim -0.0003$. The dynamics of rotation will be detailed with respect to the momentum transport processes in a separate publication.

Finally, statistical properties are assessed for $300 \leq tv_{\mathrm{ti}}/R_0 \leq 750$ with a radial average in the source free region ($0.5 \leq \rho \leq 0.8$). Figures 18(a) and 18(b) show the frequency Fourier spectrum of ion turbulent energy flux Q_i/Q_{GB} and normalized temperature gradient R_0/L_{ti}, with the gyro-Bohm coefficient $Q_{\mathrm{GB}} = n_i T_i v_{\mathrm{ti}} \rho_{\mathrm{ti}}^2/a^2$. The signal is Fourier transformed first at each radial point and then radially averaged. As discussed in Ref. 38, the frequency Fourier spectrum exhibits a $1/f$ decay at intermediate frequencies, which are found in both codes [See Fig. 18(a)]. In addition, there appears to be a transition from $1/f$ to $1/f^3$ decay at high frequencies. The transition frequency which may be interpreted as the transition from avalanche-like dynamics to vortex dynamics is the same in the two codes.

A $1/f$ decay is often considered as a typical feature of a self-organized criticality (SOC) like behavior, similar to the sand pile automaton model by Bak *et al.*[39] This agreement in the statistical properties indicates that both codes exhibit a SOC-like behavior, which stems from the nonlinear interactions between the background profile and the plasma turbulence, which is the heart of full-F gyrokinetic simulations. These findings are non-trivial since they confirm that this SOC-like behavior is robust and not dependent on numerics.

The burst characteristics can also be extracted from the probability density function (PDF) shown in Figs. 18(c) and 18(d). The PDF is obtained from the histogram with an appropriate normalization so that the integral over the range is equal to one. Although the PDF of normalized temperature gradient R_0/L_{ti} in Fig. 18(d) shows the Gaussian-like characteristic, the heat flux Q_i in Fig. 18(c) shows the long-tails in both codes indicating the non-Gaussian transport phenomena. It should still be noted that the heat flux stems from cross-correlated fluctuating quantities (temperature and $E \times B$ velocity) so that it can show non-Gaussian PDF as long as both temperature and $E \times B$ velocity exhibit Gaussian PDF.[40]

VII. SUMMARY

In this work, we have performed benchmark tests of global ITG turbulence with a fixed heat source. For this purpose, we employed two different full-F gyrokinetic codes GYSELA and GT5D. The successful benchmark of full-F global gyrokinetic codes gives confidence in the transport phenomena described by full-F models in the presence of a fixed heat source. Since the flux-driven ITG turbulence involves a wide range of physics, i.e., turbulence, neoclassical and their interplay, it is not easy to perform benchmarking straight away for a flux driven case. Thus, we first decomposed the problem into small subsets that correspond to idealized physical situations. Basically, the equilibrium poloidal flow is described by the neoclassical physics and the time evolution of turbulence is described by the gyrokinetic model. For the benchmarking of neoclassical physics,

we choose the plasma parameters such that ITG modes are stable. For the benchmarking of turbulence, we investigated the linear ITG modes and decaying ITG turbulence in the weak collisional regime. After getting a reasonable agreement, we carried out a flux-driven benchmark with the appropriate numerical and physical settings.

First, we carried out the benchmark of neoclassical theory and zonal flow damping tests. Neoclassical theory predicts the ion heat transport level and the mean poloidal velocity. In order to compare the simulation results against theory, we carried out a collisionality scan for a wide range of $\nu_* = 0.01 - 10.0$ and confirmed that both codes give the ion heat transport predicted by theory. In combination with the radial force balance relation, we confirmed that the poloidal velocity agrees well with the theoretical estimate. The short and long time behaviors of the zonal flows are also compared against theory. For short time behavior, it is confirmed that the GAM frequency and the damping rate agree with the theoretical estimate. The long time behavior called the residual zonal flow is also investigated and compared with the Rosenbluth-Hinton theory. Both codes show the convergence of the zonal flow velocity to the level predicted by theory. Thanks to the benchmarking above, we got ready to carry out the long-time flux-driven simulations with collisions. The long time zonal flow behavior is particularly important since the flux-driven simulations require robust long-time behaviors.

Second, we carried out benchmarks for linear ITG modes and nonlinear decaying ITG turbulence to test the gyrokinetic model. In the linear benchmark, we found good agreements for the growth rates and real frequencies. Also, we found a similar shape of the global eigenmodes. The analysis for the nonlinear decaying ITG turbulence shows good agreements in the critical temperature gradients. Although pure collisionless situations would be preferable, a weak collision has been added in order to avoid unphysical solutions due to the absence of diffusion in $v_{\|}$ direction, whose impact on the turbulence is confirmed to be negligible in the decaying turbulence case. It was also found that the radial structures of the zonal flow and the temperature gradient have quite similar features. In the asymptotic state, turbulence heat transport is almost quenched and the temperature gradient is below the critical level.

Finally, a benchmarking of long-time flux-driven simulations has been performed. As described above, this kind of simulation includes every single piece of physics benchmarked above. The spatio-temporal evolutions of ion turbulent heat flux showed an avalanche-like transport in both codes. Correspondingly, we found avalanche-like features in the temperature gradient and electric field shear. We also found an ion temperature profile constrained by the nonlinear threshold of L_{ti} value. In addition, we compared the radial electric field to find a global V-shape with a negative peak around the mid-minor radius. Although the amplitude is not the same, we found co-current rotation near the core and counter-current rotation near the edge in both codes. We found similar statistical properties, like $1/f$ decay and its transition to $1/f^3$ decay in both codes. These features can be considered as indicative of a self-organized criticality (SOC) behavior, which are the heart of the full-F flux driven gyrokinetic simulations. These simulations confirm that this SOC-like behavior is robust and independent of numerics.

In addition to the presented comparisons, it may be useful to report the difficulties we encountered in this benchmarking work. Indeed, there are mainly three important points: boundary conditions for the electrostatic potential, initial conditions, and sink terms.

1. Boundary conditions are critical in the Rosenbluth-Hinton test (see Sec. IV B). The radial wavenumber k_r of zonal mode can evolve in time which results in a time evolution of GAM damping rate [see Eq. (2.10) in Ref. 31 for the dependence of GAM damping rate on k_r]. Since boundary conditions have large impacts on the time evolution of k_r, it is important to give the appropriate boundary conditions for the two codes.
2. Nonlinear simulations are sensitive to initial conditions. Especially, the amplitude and time behavior of avalanche-like transport in flux-driven simulations are chaotic. This complex dynamics is sensitive to initial conditions.[33] In addition, GYSELA and GT5D employ different numerical schemes so that we cannot expect an exact agreement in the spatio-temporal turbulence behavior. Nevertheless, one may expect the system to be insensitive to initial conditions after several confinement time, but it is generally too costly and cannot be tackled in the present study. Rather, we compare the statistical properties like PDF and frequency spectra, for which we can expect an agreement as discussed in Ref. 33. This is the reason why it is important to analyse statistical properties in flux-driven simulation benchmarking. The decaying turbulence is also largely affected by initial conditions, where we compare well-defined properties like the critical temperature gradient and the relaxation process toward the asymptotic state.
3. The sink model implementation is also a matter. Comparing two different flux-driven simulations with diffusion or Krook operators by GYSELA, it turned out that these operators give different toroidal flow and radial electric field profiles. In fact, a Krook-type sink term works not only as a heat sink but also work as a momentum source (sink) term when a negative (positive) momentum flux is absorbed. Therefore, using the same sink operator is also quite important to get the similar toroidal flow profile. As a matter of fact, much effort is now devoted to the development of physically more relevant boundaries, including the modeling of the open field line region (Scrape-Off Layer).[23]

As is clear, all the points presented above should be appropriately treated for the benchmark of flux-driven simulations.

ACKNOWLEDGMENTS

All the simulations were performed on Helios at IFERC and Marconi at CINECA. The authors thank Ch. Passeron for technical support on performing large-scale simulations on these supercomputers. This work was partly supported by

the MEXT, Grant for HPCI Strategic Program Field No. 4: Next-Generation Industrial Innovations, and Grant for Post-K priority issue No. 6: Development of Innovative Clean Energy. This work has also received funding from the European Union's Horizon 2020 research and innovation programme under Grant Agreement No. 633053. The views and opinions expressed herein do not necessarily reflect those of the European Commission.

APPENDIX: COMPARISON OF NUMERICAL COSTS

It is good to know the difference in numerical costs of these two codes to understand more about the algorithm efficiencies, i.e., Semi-Lagrangian scheme in GYSELA and Finite-Difference scheme in GT5D. In order to consider the efficiency from the view point of time-to-solution, we employ Lattice Update Per Second (LUPS) as a metric rather than Floating-point Operations Per Second (FLOPS). LUPS is computed by the number of grids divided by an elapsed time for updating each grid point.

Both GYSELA and GT5D codes are highly parallelized and based on a hybrid MPI/OpenMP programming model.[41,42] The parallelization strategies are to some extent similar where both codes define a MPI communicator for each value of the magnetic moment μ. This strategy reflects the underlying physics that the magnetic moment μ is a parameter in Vlasov equation if we dismissed the collisional effects [see Eqs. (1)–(3)]. Thus, the number of sub-domains in μ direction p_μ is equivalent to N_μ the mesh size of μ direction. Inside each μ communicator, the two dimensional domain decomposition is applied to the poloidal plane (N_x, N_y). If we call the number of sub-domains in (x, y) directions (p_x, p_y), the original domain (N_x, N_y) is decomposed into a sub-domain sized $(N_x/p_x, N_y/p_y)$. Here, (x, y) represents (r, θ) in GYSELA and (R, Z) in GT5D as described in Sec. III C. The total number of MPI processes can be written as $N_{\mathrm{MPI}} = p_x \times p_y \times N_\mu$.

To investigate the strong scaling, we scan with the number of sub-domains ranged $(p_r, p_\theta) = (1\text{–}4, 1\text{–}4)$ in GYSELA and $(p_R, p_Z) = (2\text{–}8, 2\text{–}8)$ in GT5D. The sub-domain in μ direction and the number of threads $(N_\mu, N_{\mathrm{thread}})$ are kept constant with $(16, 18)$ in GYSELA and $(16, 4)$ in GT5D. As a testbed, we employ the Intel Xeon Processor E5–2697 V4[43] (Broadwell family) equipped with 18 cores. Hyperthreading is switched off in this test. The different configuration of GYSELA and GT5D in the number of cores per CPU is coming from the measured performance of GT5D (GYSELA uses 18 cores per CPU, while GT5D uses 16 cores per CPU). It is also possible to use the same parallelization in GT5D as GYSELA, but we found a slightly higher performance with 16 cores per CPU (more MPI processes and less OpenMP threads). This can be partially explained by a higher cache locality with the MPI-domain decomposition inside a CPU. It should be noted that our codes have been optimized for Sandy Bridge architecture, not for Broadwell architecture which is used in this study. Therefore, the results shown here cannot be considered as fully optimized, but moderately optimized. Figure 19 shows the strong and weak scaling of both codes obtained from the flux-driven simulations with $\rho_*^{-1} = 100$ and $\rho_*^{-1} = 150$ on the Marconi supercomputer.[44] The input power is set as 1.33 MW for $\rho_*^{-1} = 100$ and 2 MW for $\rho_*^{-1} = 150$, which also scales with plasma size in order to keep the plasma parameter as close as possible. The $\rho_*^{-1} = 100$ case is resolved with a mesh size $(N_x, N_y, N_\varphi, N_{v_\parallel}, N_\mu) = (128 \times 128 \times 32 \times 128 \times 16)$ and the $\rho_*^{-1} = 150$ case is resolved with a mesh $(N_x, N_y, N_\varphi, N_{v_\parallel}, N_{v_\perp}) = (256 \times 256 \times 32 \times 128 \times 16)$. The time step size is set as $\Delta t \Omega_i = 10$ in GYSELA and 5 in GT5D for each case. The elapsed time for Lattice Update is measured by the total elapsed time excluding diagnostics and initialization divided by the number of iterations.

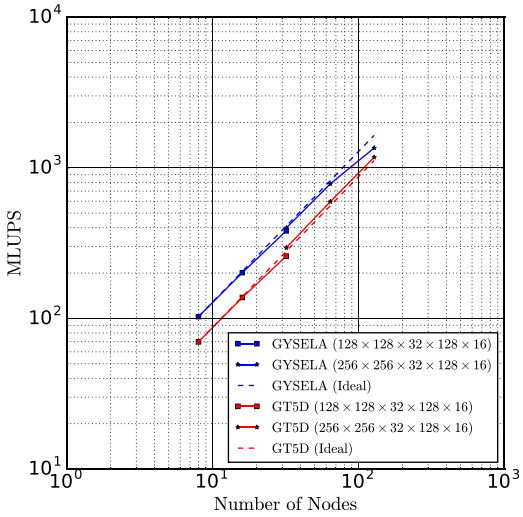

FIG. 19. Mega Lattice Update Per Seconds (MLUPS) of both codes. For problem sizes, we employed the small one for $\rho_*^{-1} = 100$ with $(N_x, N_y, N_\varphi, N_{v_\parallel}, N_\mu) = (128 \times 128 \times 32 \times 128 \times 16)$ and the middle one for $\rho_*^{-1} = 150$ with $(N_x, N_y, N_\varphi, N_{v_\parallel}, N_\mu) = (256 \times 256 \times 32 \times 128 \times 16)$. For a parallelization configuration, we employ $(p_r, p_\theta, N_\mu, N_{\mathrm{thread}}) = (1\text{–}4, 1\text{–}4, 16, 18)$ for GYSELA and $(p_R, p_Z, N_\mu, N_{\mathrm{thread}}) = (2\text{–}8, 2\text{–}8, 16, 4)$ for GT5D. One node includes two Broadwell CPUs.

In GYSELA, the 4D advection solver occupies about 65% of the overall execution cost, which consists of the 2D $(r, \theta) + 1\mathrm{D}\ (v_\parallel) + 1\mathrm{D}\ (\varphi)$ interpolation (50%) and the transpose communication (15%). The most time-consuming part of the rest is the collision operator which corresponds to about 20% of the total cost. For the interpolation, GYSELA employs the cubic spline interpolation method, which has a good conservation property at the cost of non-locality. Due to the non-local feature, a single MPI process should have an access to all the values of a distribution function f in a dimension where the interpolation takes place. Therefore, for the 2D interpolation in (r, θ) directions, a transpose communication is required to construct the original (r, θ) domain from each sub-domain in (r, θ) directions kept by a single MPI process.

In GT5D, the iterative solver for linear advection term costs about 90% of the total elapsed time, which is solved implicitly with the 4th-order 4D Finite-Difference scheme. The collision operator costs about 5% of the total cost. The asymmetric block diagonal matrix is solved with the generalized conjugate residual (GCR) method. Since the matrix solver requires several iterations, this is the most time consuming part, which consists of the 4th-order 4D

Finite-Difference computation (35%) and the vector computations (55%) such as DAXPY and DDOT. The Finite-Difference part includes the halo-communication (5%) and the vector computation part includes the inter-node all-reduce communication (5%).

As shown in Fig. 19, it is found that GYSELA is faster than GT5D about 30%–40% for small number of nodes and 15% for 128 nodes. This represents the better overall performance of GYSELA and better scalability of GT5D. The better performance of GYSELA can be interpreted as higher computational intensity of the advection solver, which could be an important advantage for Semi-Lagrangian method. Higher computational intensity could be especially important on the recent architectures like Broadwell which have a high computational performance and a relatively low memory bandwidth. The GT5D weak scaling from $\rho_*^{-1} = 100$ to $\rho_*^{-1} = 150$ shows a super scaling, which stems from the difference in the number of iterations required by GCR method. It should be noted that the number of iterations cannot be fixed and different plasma parameters result in different numbers of iterations. The better scalability of GT5D can be explained by communication-computation overlapping based on OpenMP[42] (allocating the master thread to communication and others to computation), which is applied to hide the halo-communication cost in the Finite-Difference part. In order to reduce the inter-node all-reduce communication cost, communication avoiding algorithms[45] could be applied in the future. Similar strategy for communication-computation overlapping could be applied to GYSELA, by pipelining the advection part to overlap the small chunks of transpose communications and advection computations.

[1]X. Garbet, Y. Idomura, L. Villard, and T. Watanabe, Nucl. Fusion **50**, 043002 (2010).
[2]A. M. Dimits, G. Bateman, M. A. Beer, B. I. Cohen, W. Dorland, G. W. Hammett, C. Kim, J. E. Kinsey, M. Kotschenreuther, A. H. Kritz, L. L. Lao, J. Mandrekas, W. M. Nevins, S. E. Parker, A. J. Redd, D. E. Shumaker, R. Sydora, and J. Weiland, Phys. Plasmas **7**, 969–983 (2000).
[3]W. M. Nevins, J. Candy, S. Cowley, T. Dannert, A. Dimits, W. Dorland, C. Estrada-Mila, G. W. Hammett, F. Jenko, M. J. Pueschel, and D. E. Shumaker, Phys. Plasmas **13**, 122306 (2006).
[4]G. Dif-Pradalier, P. H. Diamond, V. Grandgirard, Y. Sarazin, J. Abiteboul, X. Garbet, P. Ghendrih, A. Strugarek, S. Ku, and C. S. Chang, Phys. Rev. E **82**, 025401 (2010).
[5]G. Dif-Pradalier, G. Hornung, X. Garbet, P. Ghendrih, V. Grandgirard, G. Latu, and Y. Sarazin, Nucl. Fusion **57**, 066026 (2017).
[6]S. Ku, C. Chang, and P. Diamond, Nucl. Fusion **49**, 115021 (2009).
[7]F. Jenko, Comput. Phys. Commun. **125**, 196–209 (2000).
[8]S. Jolliet, A. Bottino, P. Angelino, R. Hatzky, T. Tran, B. Mcmillan, O. Sauter, K. Appert, Y. Idomura, and L. Villard, Comput. Phys. Commun. **177**, 409–425 (2007).
[9]V. Grandgirard, Y. Sarazin, P. Angelino, A. Bottino, N. Crouseilles, G. Darmet, G. Dif-Pradalier, X. Garbet, P. Ghendrih, S. Jolliet, G. Latu, E. Sonnendrücker, and L. Villard, Plasma Phys. Controlled Fusion **49**, B173 (2007).
[10]Y. Idomura, M. Ida, T. Kano, N. Aiba, and S. Tokuda, Comput. Phys. Commun. **179**, 391–403 (2008).
[11]G. L. Falchetto, B. D. Scott, P. Angelino, A. Bottino, T. Dannert, V. Grandgirard, S. Janhunen, F. Jenko, S. Jolliet, A. Kendl, B. F. McMillan, V. Naulin, A. H. Nielsen, M. Ottaviani, A. G. Peeters, M. J. Pueschel, D. Reiser, T. T. Ribeiro, and M. Romanelli, Plasma Phys. Controlled Fusion **50**, 124015 (2008).
[12]X. Lapillonne, B. F. McMillan, T. Görler, S. Brunner, T. Dannert, F. Jenko, F. Merz, and L. Villard, Phys. Plasmas **17**, 112321 (2010).
[13]V. Grandgirard, J. Abiteboul, J. Bigot, T. Cartier-Michaud, N. Crouseilles, G. Dif-Pradalier, C. Ehrlacher, D. Estève, X. Garbet, P. Ghendrih, G. Latu, M. Mehrenberger, C. Norscini, C. Passeron, F. Rozar, Y. Sarazin, E. Sonnendrücker, A. Strugarek, and D. Zarzoso, Comput. Phys. Commun. **207**, 35–68 (2016).
[14]Y. Idomura, J. Comput. Phys. **313**, 511–531 (2016).
[15]A. J. Brizard and T. S. Hahm, Rev. Mod. Phys. **79**, 421–468 (2007).
[16]Y. Idomura, H. Urano, N. Aiba, and S. Tokuda, Nucl. Fusion **49**, 065029 (2009).
[17]S. Satake, Y. Idomura, H. Sugama, and T.-H. Watanabe, Comput. Phys. Commun. **181**, 1069–1076 (2010).
[18]G. Dif-Pradalier, P. H. Diamond, V. Grandgirard, Y. Sarazin, J. Abiteboul, X. Garbet, P. Ghendrih, G. Latu, A. Strugarek, S. Ku, and C. S. Chang, Phys. Plasmas **18**, 062309 (2011).
[19]D. Estève, X. Garbet, Y. Sarazin, V. Grandgirard, T. Cartier-Michaud, G. Dif-Pradalier, P. Ghendrih, G. Latu, and C. Norscini, Phys. Plasmas **22**, 122506 (2015).
[20]D. Estève, Y. Sarazin, X. Garbet, V. Grandgirard, S. Breton, P. Donnel, Y. Asahi, C. Bourdelle, G. Dif-Pradalier, C. Ehrlacher, C. Emeriau, P. Ghendrih, C. Gillot, G. Latu, and C. Passeron, "Self-consistent gyrokinetic modeling of neoclassical and turbulent impurity transport," Nucl. Fusion (published online).
[21]A. Lenard and I. B. Bernstein, Phys. Rev. **112**, 1456–1459 (1958).
[22]X. Q. Xu and M. N. Rosenbluth, Phys. Fluids B: Plasma Phys. **3**, 627–643 (1991).
[23]G. Dif-Pradalier, E. Caschera, P. Ghendrih, Y. Asahi, P. Donnel, X. Garbet, V. Grandgirard, G. Latu, C. Norscini, and Y. Sarazin, Plasma Fusion Res. **12**, 1203012 (2017).
[24]G. Strang, SIAM J. Numer. Anal. **5**, 506–517 (1968).
[25]Y. Morinishi, T. Lund, O. Vasilyev, and P. Moin, J. Comput. Phys. **143**, 90–124 (1998).
[26]L. Ming-Chih, Numer. Methods Partial Diff. Eqs. **17**, 199–203 (2001).
[27]N. Bouzat, C. Bressan, V. Grandgirard, G. Latu, and M. Mehrenberger, "Targeting realistic geometry in Tokamak code Gysela," Proceedings of the ESAIM (to be published).
[28]C. S. Chang and F. L. Hinton, Phys. Fluids **25**, 1493–1494 (1982).
[29]F. L. Hinton and R. D. Hazeltine, Rev. Mod. Phys. **48**, 239–308 (1976).
[30]M. N. Rosenbluth and F. L. Hinton, Phys. Rev. Lett. **80**, 724–727 (1998).
[31]H. Sugama and T.-H. Watanabe, J. Plasma Phys. **72**, 825–828 (2006).
[32]C. Greenfield, J. DeBoo, T. Osborne, F. Perkins, M. Rosenbluth, and D. Boucher, Nucl. Fusion **37**, 1215 (1997).
[33]S. Jolliet and Y. Idomura, Nucl. Fusion **52**, 023026 (2012).
[34]F. Rath, A. G. Peeters, R. Buchholz, S. R. Grosshauser, P. Migliano, A. Weikl, and D. Strintzi, Phys. Plasmas **23**, 052309 (2016).
[35]A. G. Peeters, F. Rath, R. Buchholz, Y. Camenen, J. Candy, F. J. Casson, S. R. Grosshauser, W. A. Hornsby, D. Strintzi, and A. Weikl, Phys. Plasmas **23**, 082517 (2016).
[36]M. Kikuchi and M. Azumi, Rev. Mod. Phys. **84**, 1807–1854 (2012).
[37]B. F. McMillan, S. Jolliet, T. M. Tran, L. Villard, A. Bottino, and P. Angelino, Phys. Plasmas **16**, 022310 (2009).
[38]Y. Sarazin, V. Grandgirard, J. Abiteboul, S. Allfrey, X. Garbet, P. Ghendrih, G. Latu, A. Strugarek, G. Dif-Pradalier, P. Diamond, S. Ku, C. Chang, B. McMillan, T. Tran, L. Villard, S. Jolliet, A. Bottino, and P. Angelino, Nucl. Fusion **51**, 103023 (2011).
[39]P. Bak, C. Tang, and K. Wiesenfeld, Phys. Rev. Lett. **59**, 381–384 (1987).
[40]B. A. Carreras, C. Hidalgo, E. Sánchez, M. A. Pedrosa, R. Balbìn, I. Garcìa-Cortés, B. van Milligen, D. E. Newman, and V. E. Lynch, Phys. Plasmas **3**, 2664–2672 (1996).
[41]J. Bigot, V. Grangirard, G. Latu, C. Passeron, F. Rozar, and O. Thomine, in Proceedings of the ESAIM (2013), Vol. **43**, pp. 117–135.
[42]Y. Idomura, M. Nakata, S. Yamada, M. Machida, T. Imamura, T. Watanabe, M. Nunami, H. Inoue, S. Tsutsumi, I. Miyoshi, and N. Shida, Int. J. High Performance Comput. Appl. **28**, 73–86 (2014).
[43]See http://ark.intel.com/products/91755/Intel-Xeon-Processor-E5-2697-v4-45M-Cache-2_30-GHz for Intel® Xeon® *Processor E5-2697 v4 (45M Cache, 2.30 GHz)*.
[44]See http://www.hpc.cineca.it/news/marconi-new-cineca-supercomputer for *MARCONI: the new Cineca supercomputer*.
[45]M. Hoemmen, "Communication-avoiding Krylov subspace methods," Ph.D. thesis (EECS Department, University of California, Berkeley, 2010).